GEOPHYSICS, VOL. 52, NO. 7 (JULY 1987); P. 943-964, 20 FIGS.

A new slant on seismic imaging: Migration and integral geometry

D. Miller*, M. Oristaglio*, and G. Beylkin*

ABSTRACT

A new approach to seismic migration formalizes the classical diffraction (or common-tangent) stack by relating it to linearized seismic inversion and the generalized Radon transform. This approach recasts migration as the problem of reconstructing the earth's acoustic scattering potential from its integrals over isochron surfaces. The theory rests on a solution of the wave equation with the geometrical-optics Green function and an approximate inversion formula for the generalized Radon transform.

The method can handle both complex velocity models and (nearly) arbitrary configurations of sources and receivers. In this general case, the method can be implemented as a weighted diffraction stack, with the weights determined by tracing rays from image points to the experiment's sources and receivers. When tested on a finite-difference simulation of a deviated-well vertical seismic profile (a hybrid experiment which is difficult to treat with conventional wave-equation methods), the algorithm accurately reconstructed faulted-earth models.

Analytical reconstruction formulas are derived from the general formula for zero-offset and fixed-offset surface experiments in which the background velocity is constant. The zero-offset inversion formula resembles standard Kirchhoff migration.

Our analysis provides a direct connection between the experimental setup (source and receiver positions, source wavelet, background velocity) and the spatial resolution of the reconstruction. Synthetic examples illustrate that the lateral resolution in seismic images is described well by the theory and is improved greatly by combining surface data and borehole data. The best resolution is obtained from a zero-offset experiment that surrounds the region to be imaged.

INTRODUCTION

Traditionally, migration has meant constructing an image of the earth from seismic reflections recorded at its surface (Robinson, 1983; Gazdag and Sguazzero, 1984). The earliest migration was graphical; it was based on geometrical ideas that can be traced back to J. C. Karcher in 1921 (see Gardner, 1985) and were developed systematically by Hagedoorn (1954). These geometrical ideas were also the basis of the first digital methods—the diffraction and common-tangent stacks of what is now called classical or statistical migration (Lindsey and Hermann, 1970; Rockwell, 1971; Schneider, 1971; Johnson and French, 1982). In the 1970s, however, classical migration was largely abandoned in favor of the wave-equation methods that Claerbout (1971) introduced. In their review article, Gazdag and Sguazzero (1984) summarize the current view "that while these [classical] migration procedures make good sense and are intuitively obvious, they are not based on a completely sound theory."

As wave-equation methods have grown in popularity, migration has come to mean reverse propagation, in which recorded waves are downward continued or propagated backward in time and the image is extracted from the wave field by an imaging condition (Berkhout, 1984; Stolt and Weglein, 1985). A problem with this approach, which was recognized early (Claerbout and Doherty, 1972; Schultz, 1976), is that migration is often done with data from composite experiments that do not satisfy a single wave equation. This problem can be overcome by modifying the wave equation or by invoking a hypothetical experiment, such as the exploding-reflector model, which simulates the data, but the correct construction is often difficult to find.

Presented at the 54th Annual International Meeting, Society of Exploration Geophysicists, Atlanta. Manuscript received by the Editor March 12, 1986; revised manuscript received December 1, 1986.
*Schlubmerger-Doll Research, Old Quarry Road, Ridgefield, CT 06877-4108.

In contrast, the classical diffraction stack always provides a straightforward procedure for imaging a point in the earth: One just stacks the data over the locus of points at which energy from the given image point could have arrived (French, 1974; Gardner et al., 1974). Problems with this method arise from its apparent dependence on the locations of sources and receivers, and on its ambiguous relation to the wave equation. Recently, in adapting the diffraction stack to borehole seismic experiments (Miller, 1983; Miller et al., 1984), we have found a new approach to seismic migration which addresses both of these issues and provides a sound theory for classical migration. This new approach decouples the forward and inverse problems in a way that retains the wave equation for analysis of the forward problem, but gives inversion algorithms that are applicable to hybrid (multisource, multireceiver) experiments where the data cannot be regarded as boundary conditions on a wave equation. It is also flexible enough to handle nearly arbitrary velocity models.

The ideas underlying our approach are summarized very simply: Seismic data at high frequencies, or in the far field, can be regarded as coming from integrals of the earth's acoustic scattering potential over surfaces determined by the velocity model. Using the terminology of medical imaging (Herman, 1980), we call these integrals "projections" of the scattering potential. A weighted diffraction stack then arises as a natural *backprojection* operator in reconstructing the scattering potential from its projections, i.e., from seismic data. The problem of reconstructing a function from its integrals over general geometric objects is part of the field of integral geometry (Gel'fand et al., 1966, 1969). When such problems involve integrals over surfaces, they are termed problems of inverting a generalized Radon transform (e.g., Helgason, 1984; Quinto, 1980). Our approach can thus be described as "migration by inversion of a generalized Radon transform" (Beylkin, 1985).

In fact, as we show here, neither a full theory of integral geometry nor of the generalized Radon transform is needed to obtain the main result. Once the geometry of the reconstruction problem has been understood, the basic inversion formula [equation (27)] follows directly from a localization of Radon's classical formula (Radon, 1917) for recovering a function from its integrals over planes (straight lines, in two dimensions). This approach was first proposed in Miller (1983) and is outlined in Miller et al. (1984). An alternative derivation and analysis of this formula were developed in Beylkin (1985), where connections with the theory of Fourier integral operators and with earlier work on the generalized Radon transform (Beylkin, 1982, 1984) are emphasized. The theory of Fourier integral operators provides a mathematical formalism for analyzing the accuracy of the inversion formula. Beylkin (1985) showed that the formula accurately images discontinuities in the scattering potential, which is the meaning normally given to seismic migration.

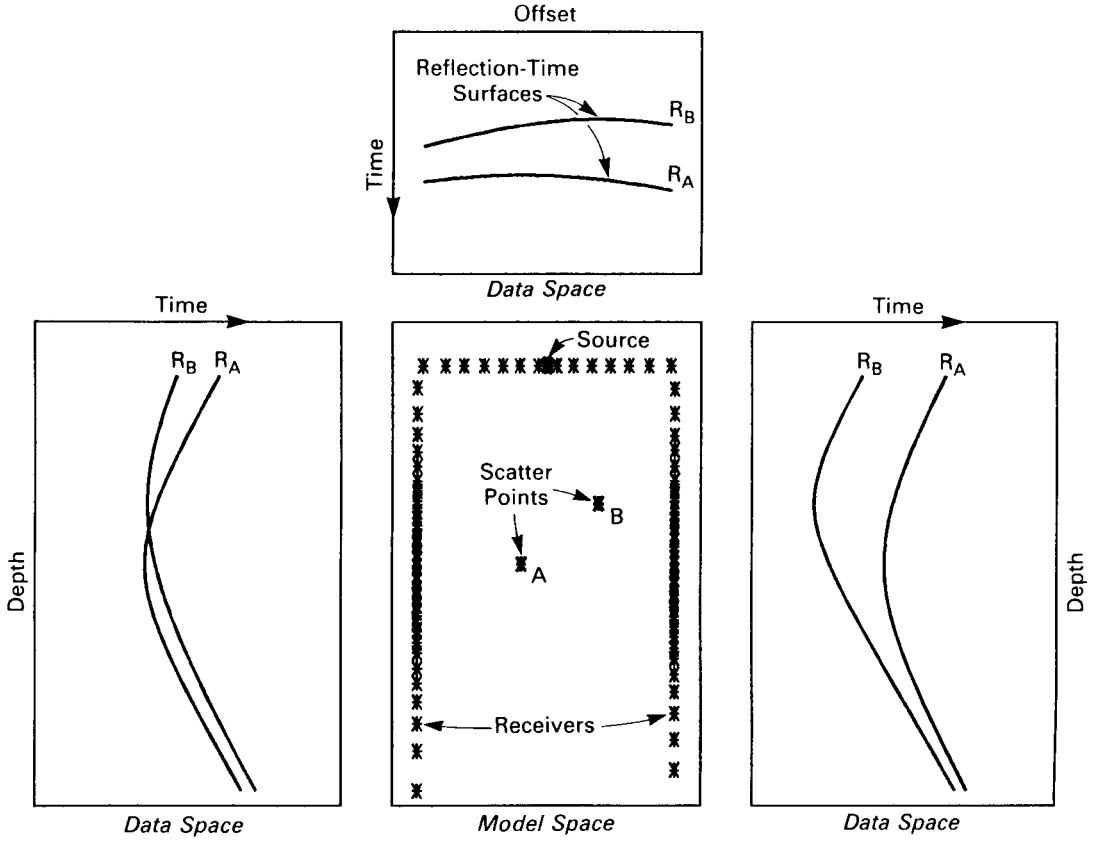

FIG. 1. Reflection-time surfaces R_A and R_B (outer panels) for two points **A** and **B** in a fixed-source experiment with receivers on the surface and in two boreholes flanking the points (inner panel). Time increases from left to right in the borehole panels; from top to bottom in the surface panel.

Development of the method described here was stimulated greatly by results given in Norton and Linzer (1981), which treated ultrasonic experiments in medical imaging. In addition to obtaining exact inversions for zero-offset experiments in a constant-background medium, Norton and Linzer (1981) recognized the analogy between acoustic scattering and the generalized Radon transform, and derived approximate imaging algorithms using backprojection of the data. Fawcett (1985) made a similar analysis of the constant-background zero-offset case and its connection to the generalized Radon transform. Our imaging method based on the generalized Radon transform is applicable to general experimental geometries and general background media.

MIGRATION AND INTEGRAL GEOMETRY

We use the following notation throughout: $\mathbf{s} = (s_1, s_2, s_3)$ represents a three-dimensional (3-D) source position, and $\mathbf{r} = (r_1, r_2, r_3)$ represents a 3-D receiver position; $\mathbf{x} = (x_1, x_2, x_3)$ and $\mathbf{y} = (y_1, y_2, y_3)$ represent typical points in a 3-D model of the earth, which we call the image or model space.

Seismic experiments yield data $u(\mathbf{r}, \mathbf{s}, t)$ which are functions of source position $\mathbf{s}$, receiver position $\mathbf{r}$, and time t (or frequency ω). A point in data space is denoted by the triplet $\mathbf{d} = (\mathbf{r}, \mathbf{s}, t)$; $u(\mathbf{d})$ is the value of the data at the point $\mathbf{d}$. As shown in this section, points in the data and image spaces are connected by the traveltime function $\tau(\mathbf{x}, \mathbf{y})$, which gives the traveltime between two points $\mathbf{x}$ and $\mathbf{y}$ within a known velocity model $c_0(\mathbf{x})$.

Geometry of classical migration

A basic principle of migration is that each point in the earth can be imaged by detecting the field scattered by that point. The most direct use of this principle was the classical diffraction stack, which evolved into wave-theoretical Kirchhoff migration (French, 1974; Schneider, 1978). The diffraction stack is a summation of the seismograms along Hagedoorn's (1954) curve of maximum convexity, also known as a diffraction curve or "*reflection-time surface*" (French, 1975). For a fixed image point $\mathbf{x}$, the reflection-time surface $R_{\mathbf{x}}$ is the locus of data points at which energy from the image point could arrive (after single scattering). Mathematically, $R_{\mathbf{x}}$ can be described as the set of triplets $\mathbf{d} = (\mathbf{r}, \mathbf{s}, t)$ in which the time t corresponds to the total traveltime from source $\mathbf{s}$, to image point $\mathbf{x}$, to receiver $\mathbf{r}$. In set notation,

$$R_{\mathbf{x}} = \left\{ \mathbf{d}: t = \tau(\mathbf{r}, \mathbf{x}) + \tau(\mathbf{x}, \mathbf{s}) \right\}. \tag{1}$$

Figure 1 depicts two reflection-time surfaces in a 2-D case where the velocity is constant, the source position is fixed, and receivers lie both along the surface and in two boreholes flanking the image points. The result of a diffraction stack along the reflection-time surface $R_{\mathbf{x}}$ has been viewed as a measure of the probability that a reflector exists at $\mathbf{x}$ (Schneider, 1971; French, 1975). Below, we reinterpret the diffraction stack as a backprojection operator that solves an integral reconstruction problem derived from the wave equation.

The counterparts of reflection-time surfaces in data space

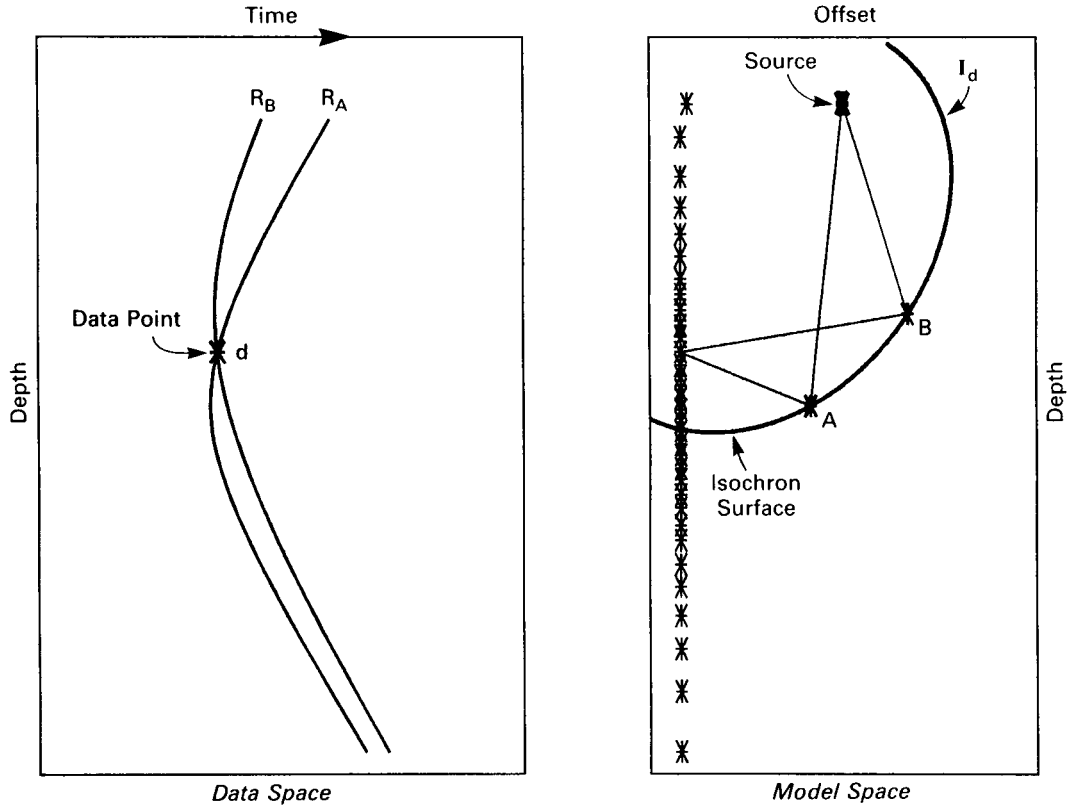

FIG. 2. Isochron surface $I_{\mathbf{d}}$ (right panel) for the data point $\mathbf{d}$ that lies at the intersection of the reflection-time surfaces R_A and R_B (left panel). Note that a point $\mathbf{x}$ belongs to $I_{\mathbf{d}}$ if and only if $\mathbf{d}$ belongs to $R_{\mathbf{x}}$.

are surfaces in model space that come from fixing a point $\mathbf{d} = (\mathbf{r}, \mathbf{s}, t)$ in the data and finding the surface of image points $\mathbf{x}$ associated with $\mathbf{d}$ by the traveltime function. We denote such a surface by $I_{\mathbf{d}}$; it is the set

$$I_{\mathbf{d}} = \left\{ \mathbf{x} : t = \tau(\mathbf{r}, \mathbf{x}) + \tau(\mathbf{x}, \mathbf{s}) \right\}. \tag{2}$$

Points in this set satisfy the constraint that the total traveltime from the source $\mathbf{s}$ to the image point $\mathbf{x}$ and to the receiver $\mathbf{r}$ is constant and equal to t. Hagedoorn (1954) called this set of points a surface of maximum concavity in the model; we call it an "*isochron surface.*" Figure 2 depicts an isochron surface for the same geometry as in Figure 1. With a constant-background velocity, an isochron surface is an ellipsoid (ellipse in two dimensions) with the source and receiver at the foci.

It is well-known that a diffraction stack can be implemented indirectly by smearing the data points $u(\mathbf{d})$ along their corresponding isochron surfaces $I_{\mathbf{d}}$. This process, commonly called backprojection, was the basis of the common-tangent stack (Rockwell, 1971; Schneider, 1971). In a common-tangent stack, the final image at a point $\mathbf{x}$ is the sum of all data points $u(\mathbf{d})$ that were backprojected along isochron surfaces passing through $\mathbf{x}$ (Figure 3). Since each isochron surface passing through $\mathbf{x}$ is associated with a data point on the reflection-time surface $R_{\mathbf{x}}$, the common tangent and diffraction stacks give the same image. The numbers are just added in a different order.

The geometrical idea embodied in equations (1) and (2) is that the traveltime τ induces a natural correspondence between points in one space and surfaces in another space. These dual geometric associations naturally give rise to a corresponding pair of projection operators (Miller, 1983):

(a) Given an *object function* $f(\mathbf{x})$ defined on the model space, we obtain a *data function* $f\hat{}(\mathbf{d})$ defined at each data point $\mathbf{d}$ by integrating f over the isochron surface $I_{\mathbf{d}}$,

$$f\hat{}(\mathbf{d}) = \int_{I_{\mathbf{d}}} f(\mathbf{x}). \tag{3}$$

(b) Given a *data function* $u(\mathbf{d})$ defined on the data space, we obtain an *object function* $u\check{}(\mathbf{x})$ defined at each model point $\mathbf{x}$ by integrating u over the reflection-time surface $R_{\mathbf{x}}$,

$$u\check{}(\mathbf{x}) = \int_{R_{\mathbf{x}}} u(\mathbf{d}).$$

The integral signs in the above expressions are symbolic and are meant to include appropriate measures for the integrations over $\mathbf{x}$ and $\mathbf{d}$. Variation of the measures gives rise to families of related operators. $f\hat{}(\mathbf{d})$ is termed the projection of the object function f over the surface $I_{\mathbf{d}}$, while $u\check{}(\mathbf{x})$ is the (back) projection of u over the surface $R_{\mathbf{x}}$.

In the following sections, we clarify the meaning of these two projection operators in the context of seismic inversion by giving precise meaning to two basic premises: (1) Seismic data $u(\mathbf{d})$ provide samples of the projections $f\hat{}$, where f is a scattering potential related to the earth's acoustic velocity profile; and (2) the scattering potential $f(\mathbf{x})$ can be approximately recovered by appropriately weighted backprojection of the data (weighted diffraction stack): $u(\mathbf{d}) \rightarrow u\check{}(\mathbf{x}) \approx f(\mathbf{x})$. The first point is implicit in the high-frequency asymptotics of acoustic scattering; it follows from using the geometrical-optics Green function in the basic integral equation for scattering. The second point is obtained from the mathematics of generalized Radon inversion. Although not treated here, a similar procedure can be derived for elastic scattering.

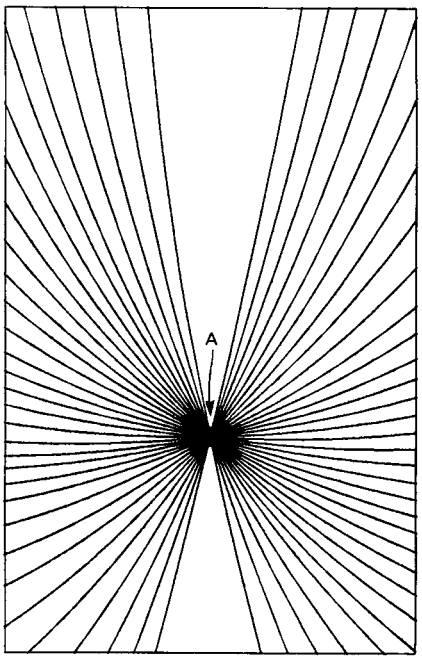

FIG. 3. Set of isochron surfaces passing through scatter point A of Figure 1 viewed in close-up perspective. The figure width represents 35 percent of the panel showing model space in Figures 1 and 2.

The acoustic generalized Radon transform

Start with the Fourier transform of the scalar wave equation for a point source,

$$\nabla^2 u(\mathbf{x}, \mathbf{s}, \omega) + \frac{\omega^2}{c^2(\mathbf{x})} u(\mathbf{x}, \mathbf{s}, \omega) = -\delta(\mathbf{x} - \mathbf{s}). \tag{4}$$

Here $u(\mathbf{x}, \mathbf{s}, \omega)$ is the total acoustic pressure field, $\mathbf{s}$ is the source position, ω is the frequency, and $c(\mathbf{x})$ is the variable acoustic velocity. The density is taken to be constant. As defined above, $u(\mathbf{x}, \mathbf{s}, \omega)$ is actually the Green function $G(\mathbf{x}, \mathbf{s}, \omega)$ for propagation in the velocity model $c(\mathbf{x})$. Given an initial estimate $c_0(\mathbf{x})$ for the velocity, split $c(\mathbf{x})$ into known and unknown parts, letting

$$c^{-2}(\mathbf{x}) = c_0^{-2}(\mathbf{x}) + f(\mathbf{x}). \tag{5}$$

The background velocity $c_0(\mathbf{x})$ need not be constant, while $f(\mathbf{x})$ is the unknown perturbation to be determined from the data. The perturbation f is called the (acoustic) scattering potential of the medium, since it is a measure of the scattering strength at points where the actual medium differs from the background medium.

Let $G_0(\mathbf{x}, \mathbf{y}, \omega)$ be the Green function for the background medium, so that

$$\nabla^2 G_0(\mathbf{x}, \mathbf{y}, \omega) + \frac{\omega^2}{c_0^2(\mathbf{x})} G_0(\mathbf{x}, \mathbf{y}, \omega) = -\delta(\mathbf{x} - \mathbf{y}). \quad (6)$$

With these definitions, equation (4) can be recast as an integral equation, analogous to the Lippman-Schwinger equation of quantum mechanics (see, e.g., Taylor, 1972),

$$u(\mathbf{y}, \mathbf{s}, \omega) = G_0(\mathbf{y}, \mathbf{s}, \omega) + \omega^2 \int d^3\mathbf{x}\, G_0(\mathbf{y}, \mathbf{x}, \omega) f(\mathbf{x}) u(\mathbf{x}, \mathbf{s}, \omega).$$

When evaluated at receiver position $\mathbf{r}$, this equation gives the observed total field as a sum of the incident field within the background model G_0 plus the scattered field, represented by the integral term. Denoting the scattered field by $u_{sc}(\mathbf{r}, \mathbf{s}, \omega) = u(\mathbf{r}, \mathbf{s}, \omega) - G_0(\mathbf{r}, \mathbf{s}, \omega)$, then

$$u_{sc}(\mathbf{r}, \mathbf{s}, \omega) = \omega^2 \int d^3\mathbf{x}\, G_0(\mathbf{r}, \mathbf{x}, \omega) f(\mathbf{x}) u(\mathbf{x}, \mathbf{s}, \omega). \quad (7)$$

Equation (7) relates the recorded data to the unknown scattering potential f. It admits the interpretation that the scattered field originates at points where the actual medium differs from the background medium through the interaction $f(\mathbf{x})u(\mathbf{x}, \mathbf{s}, \omega)$ between the scattering potential f and the total field u. The scattered wave field is then propagated by the background Green function G_0 to the receiver. Equation (7) is a nonlinear equation for f, because the total field u, which multiplies f, also depends on f. The standard technique of replacing the total field inside the integral $u(\mathbf{x}, \mathbf{s}, \omega)$ by the background or incident field $G_0(\mathbf{x}, \mathbf{s}, \omega)$ yields the linearized integral equation

$$u_{sc}(\mathbf{r}, \mathbf{s}, \omega) = \omega^2 \int d^3\mathbf{x}\, G_0(\mathbf{r}, \mathbf{x}, \omega) G_0(\mathbf{x}, \mathbf{s}, \omega) f(\mathbf{x}). \quad (8)$$

Equation (8) is a single-scattering approximation about the background medium c_0. When c_0 is constant, this equation is usually termed the (first) Born approximation. When c_0 is spatially variable, it is called the distorted-wave Born approximation (Taylor, 1972; Devaney and Oristaglio, 1984; Beylkin and Oristaglio, 1985).

The background velocity can be chosen arbitrarily in the exact equation (7), but the approximation (8) will be good only if the perturbation f is small in some sense. We assume the validity of equation (8) throughout this paper. We also assume that the Green function G_0 is available. G_0 can be written explicitly only for simple models, but numerical or asymptotic approximations can be computed for general models. For example, Clayton and Stolt (1981) considered the inversion of an equation similar to equation (8) in a layered background, where a WKBJ approximation was used for G_0 (see also Bleistein and Gray, 1985). Here, we allow arbitrary c_0 and use the first-order asymptotic approximation given by geometrical optics for G_0. Thus, we set

$$G_0(\mathbf{x}, \mathbf{y}, \omega) = A(\mathbf{x}, \mathbf{y}) e^{i\omega\tau(\mathbf{x}, \mathbf{y})},$$

where the traveltime function τ satisfies the eikonal equation

$$\left[\nabla_{\mathbf{x}} \tau(\mathbf{x}, \mathbf{y})\right]^2 = c_0^{-2}(\mathbf{x}), \quad (9)$$

and the amplitude or geometrical spreading term A satisfies the transport equation

$$A(\mathbf{x}, \mathbf{y}) \nabla_{\mathbf{x}} \tau(\mathbf{x}, \mathbf{y}) 2\nabla_{\mathbf{x}} A(\mathbf{x}, \mathbf{y}) \cdot \nabla_{\mathbf{x}} \tau(\mathbf{x}, \mathbf{y}) = 0, \quad (10)$$

along the ray connecting the points $\mathbf{x}$ and $\mathbf{y}$.

Substituting for G_0 in equation (8) gives

$$\begin{aligned} u_{sc}(\mathbf{r}, \mathbf{s}, \omega) &= \omega^2 \int d^3\mathbf{x}\, A(\mathbf{r}, \mathbf{x}) A(\mathbf{x}, \mathbf{s}) \\ &\quad \times \exp\left\{i\omega\left[\tau(\mathbf{r}, \mathbf{x}) + \tau(\mathbf{x}, \mathbf{s})\right]\right\} f(\mathbf{x}) \\ &= \omega^2 \int d^3\mathbf{x}\, A(\mathbf{r}, \mathbf{x}, \mathbf{s}) \exp\left[i\omega\tau(\mathbf{r}, \mathbf{x}, \mathbf{s})\right] f(\mathbf{x}), \end{aligned} \quad (11)$$

where we have defined $A(\mathbf{r}, \mathbf{x}, \mathbf{s})$ and $\tau(\mathbf{r}, \mathbf{x}, \mathbf{s})$ as the total amplitude and traveltime functions

$$A(\mathbf{r}, \mathbf{x}, \mathbf{s}) \equiv A(\mathbf{r}, \mathbf{x}) A(\mathbf{x}, \mathbf{s}),$$

and

$$\tau(\mathbf{r}, \mathbf{x}, \mathbf{s}) \equiv \tau(\mathbf{r}, \mathbf{x}) + \tau(\mathbf{x}, \mathbf{s}),$$

which consist of separate terms for the incident and scattered raypaths. Finally, we return to the time domain with an inverse Fourier transform, which gives

$$\begin{aligned} u_{sc}(\mathbf{r}, \mathbf{s}, t) &= -\frac{\partial^2}{\partial t^2} \int d^3\mathbf{x}\, A(\mathbf{r}, \mathbf{x}, \mathbf{s})\, \delta\left[t - \tau(\mathbf{r}, \mathbf{x}, \mathbf{s})\right] f(\mathbf{x}) \\ &= -\int d^3\mathbf{x}\, A(\mathbf{r}, \mathbf{x}, \mathbf{s})\, \delta''\left[t - \tau(\mathbf{r}, \mathbf{x}, \mathbf{s})\right] f(\mathbf{x}). \end{aligned} \quad (12)$$

The delta function in the volume integral in equation (12) collapses the spatial integration to the set of points satisfying the traveltime relation

$$t = \tau(\mathbf{r}, \mathbf{x}, \mathbf{s}) = \tau(\mathbf{r}, \mathbf{x}) + \tau(\mathbf{x}, \mathbf{s}), \quad (13)$$

that is, to points on the isochron surface $I_{\mathbf{d}}$ [see equation (2)]. Equation (12) therefore relates the scattered acoustic pressure at the data point $\mathbf{d} = (\mathbf{r}, \mathbf{s}, t)$ to the second time derivative of the weighted integral (projection) of $f(\mathbf{x})$ over the isochron surface $I_{\mathbf{d}}$,

$$u_{sc}(\mathbf{d}) = -\frac{\partial^2}{\partial t^2} \int_{I_{\mathbf{d}}} A(\mathbf{r}, \mathbf{x}, \mathbf{s}) f(\mathbf{x}). \quad (14)$$

The integral is weighted by the geometrical-spreading factors from the source to the scattering point and from the scattering point to the receiver and is differentiated twice with respect to time. Additional weighting comes from the appropriate integration measure, which is the surface measure induced by the delta function in equation (12) (Gel'fand and Shilov, 1966, p. 222). The meaning of the time derivative is illustrated in Figure 4. If the time function of the source is not a delta function, as implied by equation (4), equations (12) and (14)

will contain a convolution with the source wavelet. One can then shift the time derivative onto the source wavelet itself (see Tarantola, 1984). For reasons explained in a later section, we keep these equations in the given form. In the final section, we briefly discuss the effect of a band-limited source.

We call equation (12) [or (14)] the "acoustic GRT" and use the notation $f\hat{}$ for the integral transform itself. In terms of the projection operator defined in equation (3),

$$u_{sc}(\mathbf{d}) = -\frac{\partial^2}{\partial t^2} f\hat{}\,(\mathbf{d}).$$

A simple example of equation (12) is a 3-D model with a constant background velocity, where the geometrical-optics Green function is exactly the free-space Green function,

$$G_0(\mathbf{x}, \mathbf{y}, \omega) = \frac{\exp\left[i\omega|\mathbf{x}-\mathbf{y}|/c_0\right]}{4\pi|\mathbf{x}-\mathbf{y}|}.$$

For this case, the amplitude term $A(\mathbf{x}, \mathbf{y})$ is $1/(4\pi|\mathbf{x}-\mathbf{y}|)$, where $|\mathbf{x}-\mathbf{y}|$ is the distance between $\mathbf{x}$ and $\mathbf{y}$, and $\tau = |\mathbf{x}-\mathbf{y}|/c_0$ is the traveltime. Equation (14) becomes an integral over an ellipsoid with the source and receiver at the foci.

Analogy with the classical Radon transform

As $\mathbf{r}$, $\mathbf{s}$, and t vary over the data, the acoustic GRT gives weighted integrals of the scattering potential over isochron surfaces in the model. We derive an approximate inverse acoustic GRT by analogy with the classical Radon transform (Radon, 1917, translation in Deans, 1983).

For a 3-D function $f(\mathbf{x})$, the classical Radon transform involves integrating f over all planes. An arbitrary plane can be described as the set of points satisfying the equation $p - \xi \cdot \mathbf{x} = 0$, where ξ is a unit vector normal to the plane and p is the distance of the plane from the origin. In set notation,

$$T_{(\xi, p)} = \{\mathbf{x}: p = \xi \cdot \mathbf{x}\}.$$

The 3-D Radon transform can thus be written

$$f^{\Delta}(\xi, p) = \int_{T_{(\xi, p)}} f(\mathbf{x}) = \int d^3\mathbf{x}\, \delta(p - \xi \cdot \mathbf{x}) f(\mathbf{x}), \quad (15)$$

where we use the notation $f^{\Delta}(\xi, p)$ to denote the Radon transform of $f(\mathbf{x})$, evaluated at the data point (ξ, p).

Given the Radon transform of $f(\mathbf{x})$ for all planes $T_{(\xi, p)}$, the

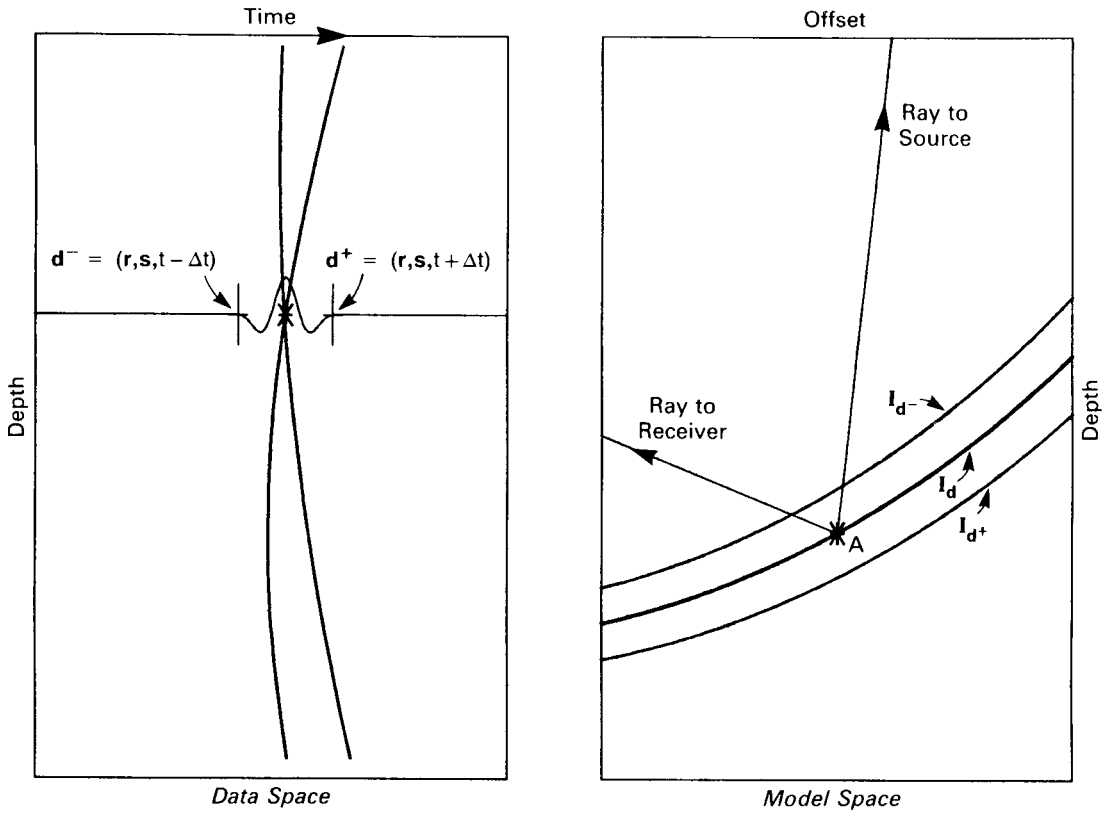

FIG. 4. The time derivative in the acoustic generalized Radon transform [equation (14)]. (left) Data point $\mathbf{d}$ (cross) and neighboring points $\mathbf{d}^+$ and $\mathbf{d}^-$. (right) The derivative needed to obtain $u_{sc}(\mathbf{d}) = u_{sc}(\mathbf{r}, \mathbf{s}, t)$ is the second derivative of integrals over parallel isochron surfaces I_d

$$u_{sc}(\mathbf{r}, \mathbf{s}, t) = \lim_{\Delta t \to 0}\left[f\hat{}(\mathbf{r}, \mathbf{s}, t + \Delta t) - 2f\hat{}(\mathbf{r}, \mathbf{s}, t) + f\hat{}(\mathbf{r}, \mathbf{s}, t - \Delta t)\right]\Big/\Delta t^2.$$

value of f at any point $\mathbf{x}_0$ can be recovered by the inversion formula (Radon, 1917; Gel'fand et al., 1966; Deans, 1983)

$$f(\mathbf{x}_0) = -\frac{1}{8\pi^2}\int d^2\xi \left[\frac{\partial^2}{\partial p^2} f^{\Delta}(\xi, p)\right]_{p=\xi\cdot\mathbf{x}_0}$$

$$= -\frac{1}{8\pi^2}\int d^2\xi \frac{\partial^2}{\partial p^2} f^{\Delta}(\xi, p = \xi\cdot\mathbf{x}_0). \qquad (16)$$

Equation (16) is the 3-D version of the filtered backprojection algorithm of X-ray tomography (see, e.g., Herman, 1980). For fixed ξ, the function $f^{\Delta}(\xi, p)$ is a one-dimensional function of p that gives the integrals of f over planes perpendicular to ξ. For any ξ, the parameter $p = p_0 = \xi\cdot\mathbf{x}_0$ marks the plane passing through a point of reconstruction $\mathbf{x}_0$. In reconstructing $f(\mathbf{x}_0)$, the transform $f^{\Delta}(\xi, p)$ is differentiated twice with respect to p and evaluated at p_0: $\partial^2 f^{\Delta}(\xi, p_0)/\partial p^2$ (the filtering step). Values of the filtered transform for all planes passing through $\mathbf{x}_0$ are then integrated with respect to $d^2\xi$, which is the solid angle measure over the unit sphere surrounding $\mathbf{x}_0$ (the backprojection step). If the unit vector ξ is specified in terms of a polar angle θ and azimuthal angle ϕ,

$$\xi = (\cos\phi \sin\theta, \sin\phi \sin\theta, \cos\theta),$$

then $d^2\xi = d\phi\, d\theta \sin\theta$. Figure 5 illustrates the geometry of the two steps in the Radon inversion algorithm.

The forward and inverse Radon transforms can be merged into an equation that is useful in developing an approximate inversion of the acoustic generalized Radon transform. From equation (15), we can write for the filtered transform

$$\frac{\partial^2}{\partial p^2} f^{\Delta}(\xi, p) = \frac{\partial^2}{\partial p^2}\int d^3\mathbf{x}\, \delta(p - \xi\cdot\mathbf{x}) f(\mathbf{x})$$

$$= \int d^3\mathbf{x}\, \delta''(p - \xi\cdot\mathbf{x}) f(\mathbf{x}).$$

Combining this with equation (16) gives

$$f(\mathbf{x}_0) = -\frac{1}{8\pi^2}\int d^2\xi \int d^3\mathbf{x}\, \delta''\Big[\xi\cdot(\mathbf{x}_0 - \mathbf{x})\Big] f(\mathbf{x}). \qquad (17)$$

The analogy between the classical Radon transform and the acoustic generalized Radon transform is easily seen. In the classical Radon transform, the unit vector ξ specifies a family of parallel planes, while the scalar parameter p fixes one plane in the family. The family of planes passing through a point $\mathbf{x}_0$ is obtained by allowing ξ to vary over the unit sphere and by taking $p = \xi\cdot\mathbf{x}_0$ for each ξ. In the acoustic generalized Radon transform, a source-receiver pair $(\mathbf{r}, \mathbf{s})$ plays the role of ξ, while the time t plays the role of the parameter p. A source-receiver pair specifies a family of "parallel" isochron surfaces (when c_0 is constant, concentric ellipsoids with $\mathbf{r}$ and $\mathbf{s}$ as common foci) and t fixes one isochron surface in the family. The family of isochron surfaces passing through a point $\mathbf{x}_0$ is obtained by allowing source and receiver positions to vary and by taking $t = \tau(\mathbf{r}, \mathbf{x}_0, \mathbf{s})$ for each $(\mathbf{r}, \mathbf{s})$ pair. These data lie on the

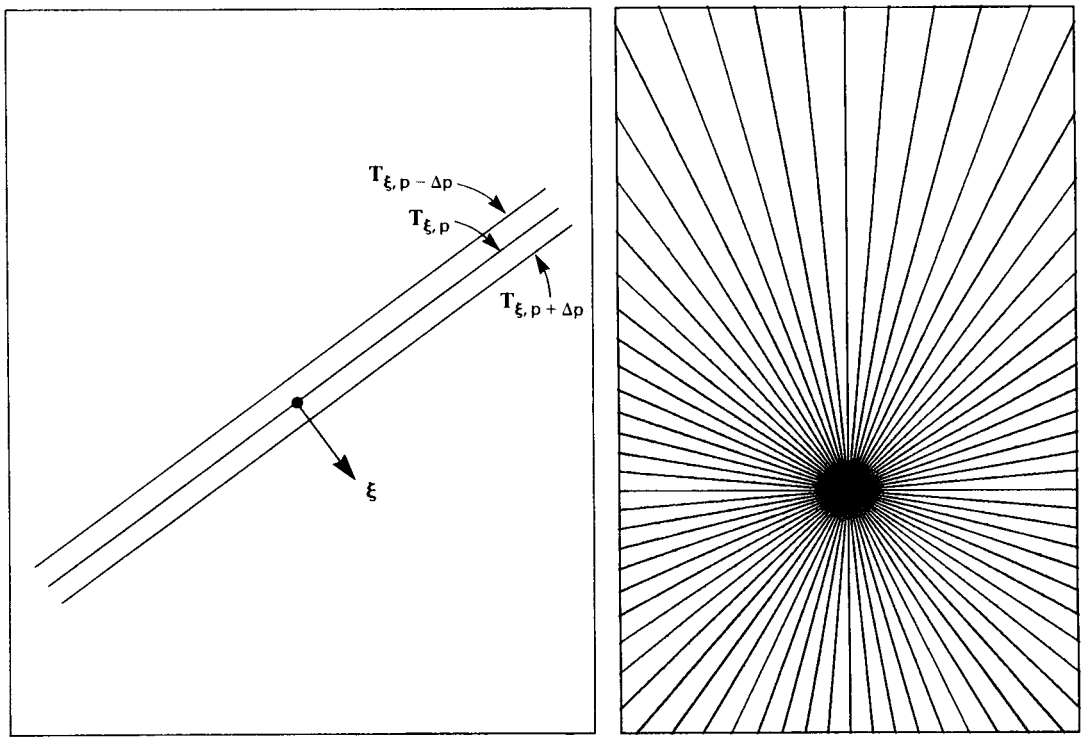

FIG. 5. Radon inversion as filtered backprojection. (left) The filter is a second derivative of integrals over parallel planes $T_{(\xi, p)}$, where the unit vector ξ is perpendicular to the planes and p parameterizes parallel planes,

$$\frac{\partial^2}{\partial p^2} f^{\Delta}(\xi, p) = \lim_{\Delta p\to 0}\Big[f^{\Delta}(\xi, p + \Delta p) - 2f^{\Delta}(\xi, p) + f^{\Delta}(\xi, p - \Delta p)\Big]\Big/\Delta p^2.$$

(right) The backprojection is an average (of the filtered transform) over planes through an image point.

reflection-time surface R_{x_0}. Note, finally, that acoustic scattering gives directly what may be called a "filtered" generalized Radon transform in which the integrals over isochron surfaces are already differentiated twice with respect to time t [compare equations (12) and (15)].

Inversion of the acoustic generalized Radon transform

An approximate inversion of the acoustic GRT can be obtained by applying the classical Radon inversion formula locally to each image point $\mathbf{x}_0$. The isochron surfaces passing through $\mathbf{x}_0$ locally resemble planes, as can be seen by comparing Figures 3 and 5. Identifying each isochron surface with its tangent plane at $\mathbf{x}_0$ and comparing equations (12), (15), and (18) suggests the following backprojection formula as an estimate $\langle f(\mathbf{x}_0)\rangle$ of the scattering potential at the point $\mathbf{x}_0$,

$$\langle f(\mathbf{x}_0)\rangle = \int dW(\mathbf{r}, \mathbf{x}_0, \mathbf{s}) \left[\frac{\partial^2}{\partial t^2} f\hat{}(\mathbf{r}, \mathbf{s}, t)\right]_{t=\tau(\mathbf{r}, \mathbf{x}_0, \mathbf{s})}$$
$$= \int dW(\mathbf{r}, \mathbf{x}_0, \mathbf{s})\, u_{sc}\left[\mathbf{r}, \mathbf{s}, t = \tau(\mathbf{r}, \mathbf{x}_0, \mathbf{s})\right]. \quad (18)$$

Equation (18) is a weighted diffraction stack, an integral of the data lying on the reflection-time surface R_{x_0}. The weighting function $dW(\mathbf{r}, \mathbf{x}_0, \mathbf{s})$ is allowed to vary for each $\mathbf{x}_0$ and represents an appropriate measure for the integral.

The identification of isochron surfaces with their tangent planes at a point $\mathbf{x}_0$ becomes precise on making some approximations in equation (12). As discussed in the Appendix, the weighted diffraction stack obtained by this identification gives an asymptotic inversion of the acoustic generalized Radon transform. To obtain the identification, first shift the origin of coordinates in the integral to the point $\mathbf{x}_0$. Letting $\mathbf{x} = \mathbf{x}_0 + \mathbf{y}$, equation (12) becomes

$$u_{sc}(\mathbf{r}, \mathbf{s}, t) = -\int d^3\mathbf{y}\, A(\mathbf{r}, \mathbf{x}_0 + \mathbf{y}, \mathbf{s})\delta''$$
$$\times \left[t - \tau(\mathbf{r}, \mathbf{x}_0 + \mathbf{y}, \mathbf{s})\right] f(\mathbf{x}_0 + \mathbf{y}). \quad (19)$$

Assume that f is localized about the point $\mathbf{x}_0$, so that $f(\mathbf{x}_0 + \mathbf{y})$ is nonzero only if $|\mathbf{y}|$ is small. We also assume that the total amplitude function A is approximately constant near $\mathbf{x}_0$ and can be moved outside the integral

$$u_{sc}(\mathbf{r}, \mathbf{s}, t) \approx -A(\mathbf{r}, \mathbf{x}_0, \mathbf{s}) \int d^3\mathbf{y}\, \delta''$$
$$\times \left[t - \tau(\mathbf{r}, \mathbf{x}_0 + \mathbf{y}, \mathbf{s})\right] f(\mathbf{x}_0 + \mathbf{y}). \quad (20)$$

We now expand the traveltime function $\tau(\mathbf{r}, \mathbf{x}, \mathbf{s})$ in a first-order Taylor series about the point $\mathbf{x}_0$,

$$\tau(\mathbf{r}, \mathbf{x}_0 + \mathbf{y}, \mathbf{s}) \approx \tau(\mathbf{r}, \mathbf{x}_0, \mathbf{s}) + \left[\nabla_{\mathbf{x}}\, \tau(\mathbf{r}, \mathbf{x}, \mathbf{s})\right]_{\mathbf{x}=\mathbf{x}_0} \cdot \mathbf{y}$$
$$\equiv \tau_0 + \nabla_{\mathbf{x}}\, \tau(\mathbf{r}, \mathbf{x}_0, \mathbf{s}) \cdot \mathbf{y}. \quad (21)$$

Here, the gradient vector of the total traveltime is the sum of gradients for the incident and scattered raypaths

$$\nabla_{\mathbf{x}}\, \tau(\mathbf{r}, \mathbf{x}_0, \mathbf{s}) = \nabla_{\mathbf{x}}\, \tau(\mathbf{r}, \mathbf{x}_0) + \nabla_{\mathbf{x}}\, \tau(\mathbf{x}_0, \mathbf{s}). \quad (22)$$

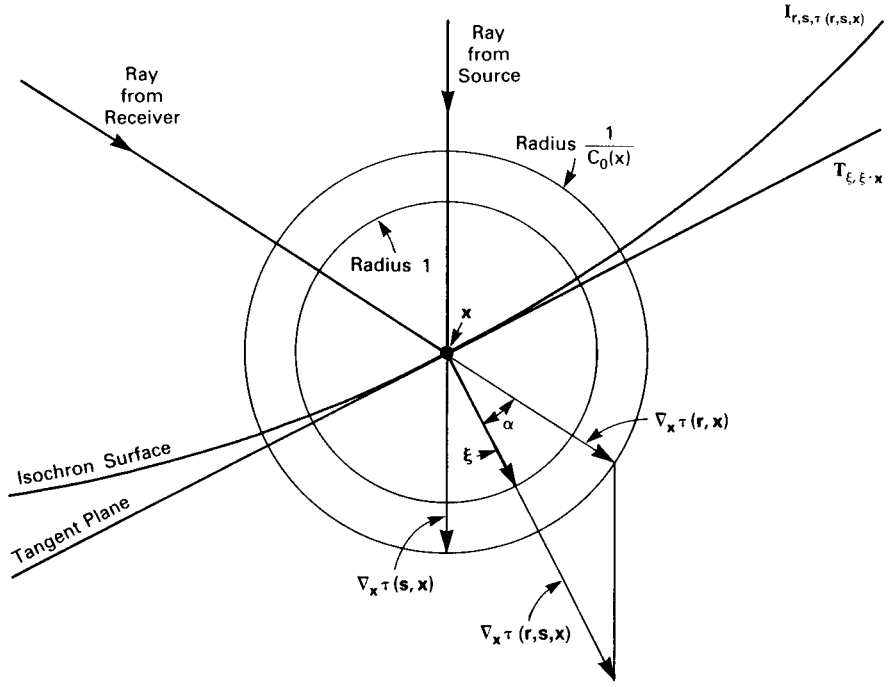

FIG. 6. The geometry matching an isochron surface with its tangent plane near an image point $\mathbf{x}$. To simplify the figure, we have omitted the subscript zero used in the text. The gradient vector $\nabla_{\mathbf{x}}\, \tau(\mathbf{x}, \mathbf{s})$ is the incident ray at $\mathbf{x}$; $\nabla_{\mathbf{x}}\, \tau(\mathbf{r}, \mathbf{x})$ is the scattered ray; α is half the angle between these two rays; ξ is a unit vector in the direction of the total traveltime gradient $\nabla_{\mathbf{x}}\, \tau(\mathbf{r}, \mathbf{x}, \mathbf{s})$.

Consider first $\nabla_x \tau(\mathbf{r}, \mathbf{x}_0)$. Since rays are perpendicular to surfaces of equal traveltime (phase) and traveltime increases as $\mathbf{x}_0$ moves away from $\mathbf{r}$, this gradient points in the opposite direction from the ray that leaves $\mathbf{x}_0$ and reaches $\mathbf{r}$ in the background model, or along the ray that arrives at $\mathbf{x}_0$ from $\mathbf{r}$. Similarly, $\nabla_x \tau(\mathbf{x}_0, \mathbf{s})$ points in the direction of the ray that arrives at $\mathbf{x}_0$ from the source $\mathbf{s}$. The geometry is illustrated in Figure 6. We call these gradient vectors the incident and scattered rays at the image point $\mathbf{x}_0$.

From the eikonal equation (9), the magnitudes of the incident and scattered rays are equal to $1/c_0(\mathbf{x}_0)$, the slowness of the background model at the point $\mathbf{x}_0$. The total traveltime gradient $\nabla_x \tau(\mathbf{r}, \mathbf{x}_0, \mathbf{s})$ lies in the plane of the incident and scattered rays at $\mathbf{x}_0$ and bisects the angle between them (Figure 6). Let α be half the angle between the incident and scattered rays; using equations (22) and (9), one finds

$$|\nabla_x \tau(\mathbf{r}, \mathbf{x}_0, \mathbf{s})| = \frac{2}{c_0(\mathbf{x}_0)} \cos \alpha \equiv \beta. \tag{23}$$

Finally, let $\xi(\mathbf{r}, \mathbf{x}_0, \mathbf{s})$ be a unit vector in the direction of the total traveltime gradient, so that

$$\nabla_x \tau(\mathbf{r}, \mathbf{x}_0, \mathbf{s}) = \beta \xi(\mathbf{r}, \mathbf{x}_0, \mathbf{s}).$$

Substituting these results into equation (19) gives

$$u_{sc}(\mathbf{r}, \mathbf{s}, \mathbf{t}) \approx -A(\mathbf{r}, \mathbf{x}_0, \mathbf{s}) \int d^3\mathbf{y}\, \delta'' \times \left[t - \tau_0 - \beta \xi(\mathbf{r}, \mathbf{x}_0, \mathbf{s}) \cdot \mathbf{y} \right] f(\mathbf{x}_0 + \mathbf{y}). \tag{24}$$

The original integrals over isochron surfaces are now approximated by integrals over planes. The unit vector $\xi(\mathbf{r}, \mathbf{x}_0, \mathbf{s})$ is normal to the planes, while time t parameterizes parallel planes. Evaluating this expression for the scattered field at a point on the reflection-time surface for $\mathbf{x}_0$, where $t = \tau_0 = \tau(\mathbf{r}, \mathbf{x}_0, \mathbf{s})$, one obtains

$$\begin{aligned} u_{sc}(\mathbf{r}, \mathbf{s}, t = \tau_0) &\approx -A(\mathbf{r}, \mathbf{x}_0, \mathbf{s}) \int d^3\mathbf{y}\, \delta'' \times \left[-\beta \xi(\mathbf{r}, \mathbf{x}_0, \mathbf{s}) \cdot \mathbf{y} \right] f(\mathbf{x}_0 + \mathbf{y}), \\ &= -\frac{A(\mathbf{r}, \mathbf{x}_0, \mathbf{s})}{|\beta|^3} \int d^3\mathbf{y}\, \delta'' \left[\xi(\mathbf{r}, \mathbf{x}_0, \mathbf{s}) \cdot \mathbf{y} \right] \times f(\mathbf{x}_0 + \mathbf{y}), \end{aligned}$$

using the relation $\delta''(-ax) = \delta''(\mathbf{x})/|a|^3$. Restoring the original variable $\mathbf{x} = \mathbf{x}_0 + \mathbf{y}$ gives

$$u_{sc}(\mathbf{r}, \mathbf{s}, t = \tau_0) \approx -\frac{A(\mathbf{r}, \mathbf{x}_0, \mathbf{s})}{|\beta|^3} \int d^3\mathbf{x}\, \delta'' \times \left[\xi(\mathbf{r}, \mathbf{x}_0, \mathbf{s}) \cdot (\mathbf{x} - \mathbf{x}_0) \right] f(\mathbf{x}). \tag{25}$$

Within the approximations leading to equation (25), the scattered data along the reflection-time surface of $\mathbf{x}_0$ are proportional to (twice-differentiated) integrals of f over planes passing through $\mathbf{x}_0$. The identification of isochron surfaces and their tangent planes is thus complete. Comparing equation (25) with the classical inversion formula [equation (17)] gives the weighting function dW directly,

$$dW(\mathbf{r}, \mathbf{x}_0, \mathbf{s}) = \frac{1}{\pi^2} d^2\xi(\mathbf{r}, \mathbf{x}_0, \mathbf{s}) \frac{|\cos^3 \alpha(\mathbf{r}, \mathbf{x}_0, \mathbf{s})|}{c_0^3(\mathbf{x}_0) A(\mathbf{r}, \mathbf{x}_0, \mathbf{s})}, \tag{26}$$

and the final inversion formula

$$\langle f(\mathbf{x}_0) \rangle = \frac{1}{\pi^2} \int d^2\xi(\mathbf{r}, \mathbf{x}_0, \mathbf{s}) \times \frac{|\cos^3 \alpha(\mathbf{r}, \mathbf{x}_0, \mathbf{s})|}{c_0^3(\mathbf{x}_0) A(\mathbf{r}, \mathbf{x}_0, \mathbf{s})} u_{sc}(\mathbf{r}, \mathbf{s}, t = \tau_0). \tag{27}$$

The inversion integral we have derived is given explicitly in terms of the angular variable ξ rather than the experimental variables $(\mathbf{r}, \mathbf{s})$. As such it represents a scheme for generating explicit inversions for various experimental configurations. Passage from the generic expression (27) to any specific version consists of evaluating the Jacobian $d^2\xi$. Formally, the mapping from ξ to the source-receiver pair $(\mathbf{r}, \mathbf{s})$, defined at each image point $\mathbf{x}_0$, must be one-to-one and differentiable. In special cases (such as those given below) it is possible to derive an explicit expression for $d^2\xi$ in terms of the experimental variables. In general numerical implementation, however, we have found it more efficient to work directly with formula (27), either by computing $(\mathbf{r}, \mathbf{s}, \tau_0)$ as a function of regularly sampled ξ, or by computing (ξ, τ_0) as a function of $(\mathbf{r}, \mathbf{s})$. In the former case, one numerically interpolates the field between its sampled values. In the latter case, one numerically computes the rate of change of ξ as its values vary according to the experimental setup and background model.

Acoustic GRT in two dimensions

The acoustic GRT and its inverse are easily modified to a 2-D world, which is useful for synthetic calculations (and for drawing pictures). In two dimensions, the geometrical-optics Green function is

$$G_0(\mathbf{x}, \mathbf{y}, \omega) = (-i\omega)^{-1/2} A(\mathbf{x}, \mathbf{y}) \exp\left[i\omega\tau(\mathbf{x}, \mathbf{y}) \right],$$

where τ and A satisfy 2-D eikonal and tranport equations. The scattering equation becomes

$$u_{sc}(\mathbf{r}, \mathbf{s}, t) = -\frac{\partial}{\partial t} \int d^2\mathbf{x}\, A(\mathbf{r}, \mathbf{x}, \mathbf{s})\, \delta\left[t - \tau(\mathbf{r}, \mathbf{x}, \mathbf{s}) \right] f(\mathbf{x}). \tag{12a}$$

The 2-D Radon inversion formula (Radon, 1917; Gel'fand et al., 1966; Deans, 1983) is

$$f(\mathbf{x}_0) = -\frac{1}{4\pi} \int d\xi\, \mathcal{H} \frac{\partial}{\partial p} f^{\Lambda}(\xi, p = \xi \cdot \mathbf{x}_0), \tag{17a}$$

where $\mathcal{H}$ denotes the Hilbert transform (principal-value integral)

$$\mathcal{H}u(t) = \frac{1}{\pi} \int_{-\infty}^{\infty} dt' \frac{u(t')}{t - t'}.$$

The analysis described above carries through with only minor changes to yield the 2-D acoustic inversion formula

$$\langle f(\mathbf{x}_0)\rangle = \frac{1}{\pi}\int d\xi(\mathbf{r}, \mathbf{x}_0, \mathbf{s}) \times \frac{\cos^2 \alpha(\mathbf{r}, \mathbf{x}_0, \mathbf{s})}{c_0^2(\mathbf{x}_0)A(\mathbf{r}, \mathbf{x}_0, \mathbf{s})} \mathscr{H} u_{sc}(\mathbf{r}, \mathbf{s}, t = \tau_0). \quad (27a)$$

Thus, the only changes are in the dimension of the integral (ξ now varies over unit vectors in the plane), in the exponent in the obliquity factor $\cos^2 \alpha$, and in the additional Hilbert transform which is applied to the scattered data before backprojection.

SPECIAL CASES

As noted, inversion formulas (27) and (27a) are suitable for direct numerical implementation; all the necessary quantities can be determined by tracing rays from image points to the experiment's sources and receivers. Nevertheless, it is instructive to derive explicit expressions in selected cases. We consider here zero-offset and fixed-offset experiments in a constant background velocity. The zero-offset migration formula was first derived in Norton and Linzer (1981) by a different approach; the fixed-offset formula was derived in Beylkin (1985).

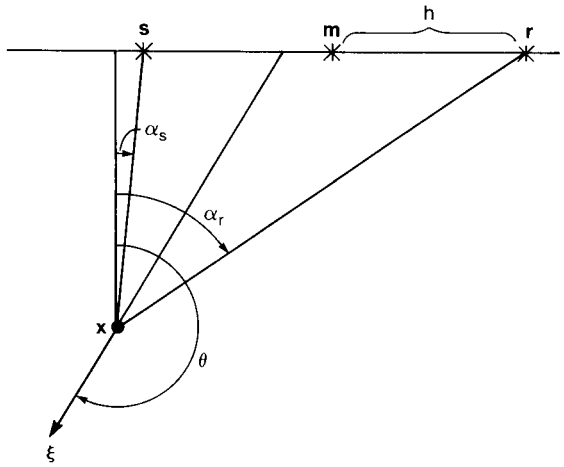

FIG. 7. Geometry of a fixed-offset experiment. α_s is the angle between the vertical and the ray from the source **s** to the image point **x**; α_r is the angle between the vertical and the ray from the receiver **r** to the image point; h is the offset. Note that the midpoint **m** between the source and receiver does not lie on the ray through ξ that bisects the source and receiver rays.

Zero-offset migration

Consider a zero-offset acoustic experiment with source-receiver pairs ("transceivers") on the surface of a half-space that contains the structure to be imaged. This geometry is commonly used to model common-midpoint stacked surface seismic data. Let $\mathbf{r} = \mathbf{s} = (r_1, r_2, r_3 = 0)$ be the position of the transceiver and let the background velocity c_0 be constant. The acoustic generalized Radon transform becomes an integration over hemispheres; the data at position **r** and time t come from an integral of $f(\mathbf{x})$ over a hemisphere centered at **r** of radius $R = c_0 t/2$. Since the rays from **r** to an image point **x** and back to **r** lie along the straight line connecting **r** and **x**, the unit vector $\xi(\mathbf{r}, \mathbf{x}, \mathbf{r})$ is

$$\xi = \frac{\mathbf{x} - \mathbf{r}}{|\mathbf{x} - \mathbf{r}|} = \frac{1}{|\mathbf{x} - \mathbf{r}|}(x_1 - r_1, x_2 - r_2, x_3). \quad (28)$$

An explicit migration formula for this case requires a change of variables from ξ to the coordinate **r** that parameterizes the experiment. For example, at any arbitrary image point **x**, specify $\xi = (\cos\phi \sin\theta, \sin\phi \sin\theta, \cos\theta)$ with polar angle θ and azimuthal angle ϕ. Substituting from equation (28) and using the relation

$$\sin\theta = \frac{x_3}{|\mathbf{x} - \mathbf{r}|}\tan\theta,$$

one finds

$$x_1 - r_1 = x_3 \tan\theta \cos\phi,$$

and

$$x_2 - r_2 = x_3 \tan\theta \sin\phi.$$

The Jacobian computation gives

$$d^2\mathbf{r} = x_3^2(1 + \tan^2\theta)(\tan\theta)\, d\theta\, d\phi = \frac{|\mathbf{x} - \mathbf{r}|^3}{x_3}\sin\theta\, d\theta\, d\phi = \frac{|\mathbf{x} - \mathbf{r}|^3}{x_3} d^2\xi.$$

The angle $\alpha(\mathbf{r}, \mathbf{x}, \mathbf{r})$ has the constant value zero, so the cosine term drops out of equation (27). Including the geometrical

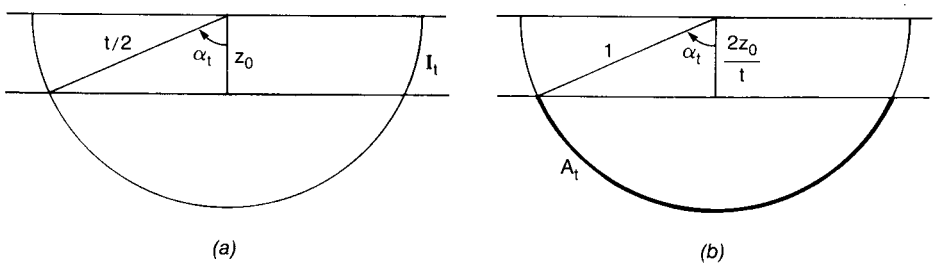

FIG. 8. Geometry for calculating zero-offset data for a reflecting half-space using the acoustic generalized Radon transform. (a) I_t is the isochron surface centered on a transceiver, with radius $t/2$. The half-space starts at $z = z_0$; α_t is the angle between the vertical and the intersection of I_t with the top of the half-space. (b) A_t is the region of a unit sphere similar to the intersection of I_t with the half-space.

factor $A(\mathbf{r}, \mathbf{x}, \mathbf{r}) = (4\pi|\mathbf{x} - \mathbf{r}|)^{-2}$ and substituting into equation (27) yields

$$\langle f(\mathbf{x})\rangle = \frac{16}{c_0^3}\int_{r_3=0} d^2\mathbf{r}\,\frac{x_3}{|\mathbf{x}-\mathbf{r}|}\,u_{sc}(\mathbf{r}, t = 2|\mathbf{x}-\mathbf{r}|/c_0)$$

$$= \frac{16}{c_0^3}\int_{r_3=0} d^2\mathbf{r}\,\cos\theta\,u_{sc}(\mathbf{r}, t = 2|\mathbf{x}-\mathbf{r}|/c_0). \quad (29)$$

A second algebraic derivation follows directly from equation (28). By definition, the surface integral

$$\int d^2\xi = \int d^2\mathbf{r}\left|\frac{\partial\xi}{\partial r_1}\times\frac{\partial\xi}{\partial r_2}\right|, \quad (30)$$

where the magnitude of the vector cross-product is the Jacobian factor. This again yields equation (29); moreover, if the data are collected on an irregular surface $r_3 = r_3(r_1, r_2)$, the only change in the derivation is that the third component of ξ becomes $x_3 - r_3(r_1, r_2)$. The latter construction works whenever it is possible to specify ξ explicitly in terms of the Cartesian coordinates of the experiment.

Fixed-offset experiments

Consider next a fixed-offset experiment on the surface of a half-space with constant background velocity. The experiment can be parameterized by the midpoint $\mathbf{m} = (m_1, m_2, 0)$ of the source-receiver pair. Let $\mathbf{h} = (h_1, h_2, 0)$ be the half-offset vector, so that the receiver position $\mathbf{r} = \mathbf{m} + \mathbf{h}$ and the source position $\mathbf{s} = \mathbf{m} - \mathbf{h}$. Then

$$\xi = \frac{1}{\left[2 + (\mathbf{x}-\mathbf{s})\cdot(\mathbf{x}-\mathbf{r})/|\mathbf{x}-\mathbf{s}|\,|\mathbf{x}-\mathbf{s}|\right]^{1/2}} \times\left(\frac{\mathbf{x}-\mathbf{r}}{|\mathbf{x}-\mathbf{r}|}+\frac{\mathbf{x}-\mathbf{s}}{|\mathbf{x}-\mathbf{s}|}\right). \quad (31)$$

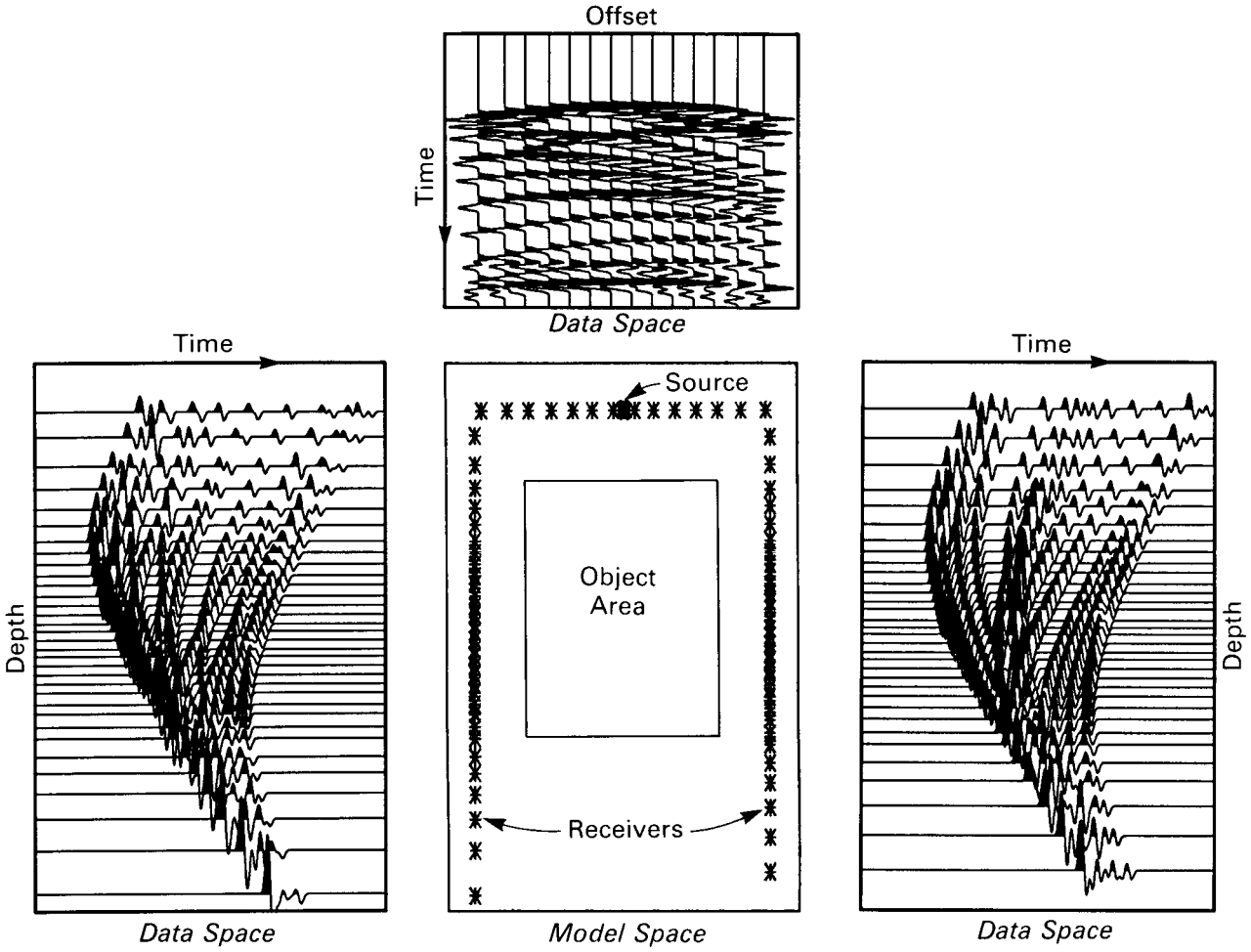

FIG. 9. Synthetic data (outer panels) from a single-source, multiple-receiver acoustic experiment with the geometry shown in the inner panel. A family of point scatterers, distributed to form the letter "S," occupies the object area, which is 350 m wide and 500 m high. The data were computed using the 2-D acoustic generalized Radon transform [equation (12a)] using a homogeneous background velocity of 2500 m/s. The source wavelet was a four-point Blackman-Harris window, with a duration of 25 ms. Time runs from 0.0 to 0.75 s. 156 traces were constructed; every second trace is displayed. Receivers 1 to 64 are in the left borehole at −250 m offset, with depths varying from 1000 m to 0 m. Receivers 65 to 91 are on the surface, with offsets varying from −250 m to +250 m. Receivers 92 to 156 are in the right borehole at 250 m offset, with depths varying from 0 m to 1000 m.

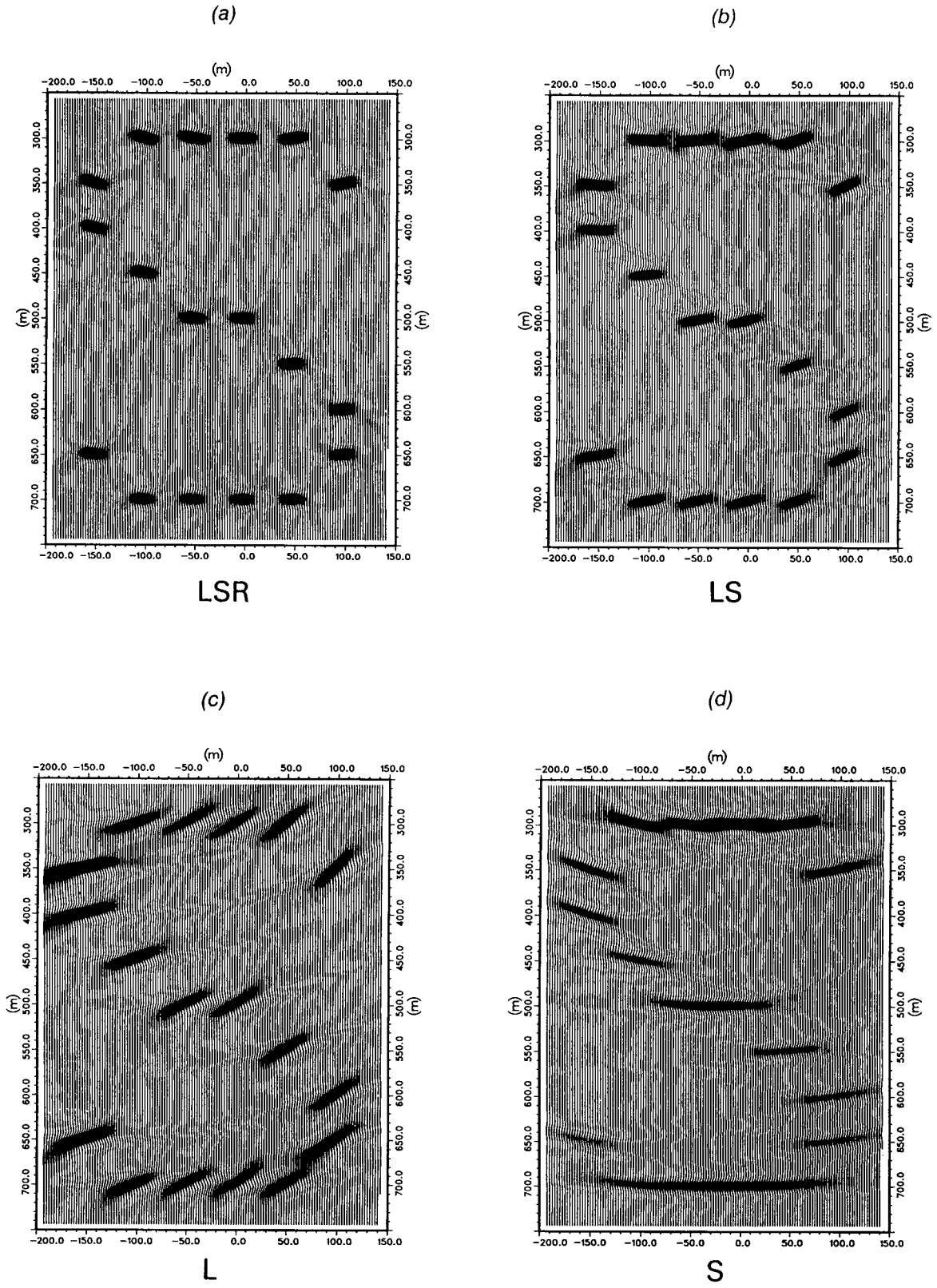

FIG. 10. Images of point scatterers occupying the object area of Figure 9. Images were obtained by applying the 2-D inverse acoustic generalized Radon transform [equation (27a)] to all the data in Figure 9 (LSR) and to the subsets of the data corresponding to the left borehole and surface (LS); left borehole only (L), and surface only (S).

A change of variables can now be made from ξ to $\mathbf{m}$ using equations (30) and (31); however, the algebra is dense. For simplicity, consider the 2-D case and work with the angular variables defined in Figure 7: the polar angle θ determines ξ, α_s is the angle between the vertical and the ray from the source to the image point $\mathbf{x}$, and α_r is the angle between the vertical and the ray from the receiver to the image point $\mathbf{x}$. Then,

$$\theta = \frac{1}{2}(\alpha_s + \alpha_r) + \pi$$

$$= \frac{1}{2}\left(\tan^{-1}\frac{m-h}{z} + \tan^{-1}\frac{m+h}{z}\right) + \pi, \qquad (32)$$

where z is the depth of the image point. Changing variables from ξ to m gives

$$d\xi = d\theta = \frac{1}{2}\left(\frac{\cos\alpha_r}{|\mathbf{x}-\mathbf{r}|} + \frac{\cos\alpha_s}{|\mathbf{x}-\mathbf{s}|}\right) dm.$$

The geometrical-optics Green function for a homogeneous 2-D medium,

$$G_0(\mathbf{x}, \mathbf{y}, \omega) = (-i\omega)^{-1/2} A(\mathbf{x}, \mathbf{y}) \exp\left[i\omega|\mathbf{x}-\mathbf{y}|/c_0\right],$$

has the amplitude factor

$$A(\mathbf{x}, \mathbf{y}) = \left(\frac{c_0}{8\pi|\mathbf{x}-\mathbf{y}|}\right)^{1/2}.$$

Thus,

$$A(\mathbf{r}, \mathbf{x}, \mathbf{s}) = \frac{c_0}{8\pi}|\mathbf{x}-\mathbf{s}|^{-1/2}|\mathbf{x}-\mathbf{r}|^{-1/2}$$

is the 2-D total-amplitude factor. Substituting into equation (27a), one obtains the inversion formula

$$\langle f(\mathbf{x})\rangle = \frac{4}{c_0^3}\int dm\left[\left(\frac{|\mathbf{x}-\mathbf{s}|}{|\mathbf{x}-\mathbf{r}|}\right)^{1/2}\cos\alpha_r + \left(\frac{|\mathbf{x}-\mathbf{r}|}{|\mathbf{x}-\mathbf{s}|}\right)^{1/2}\cos\alpha_s\right]$$

$$\times \cos^2(\alpha_r - \alpha_s)\mathscr{H}u_{sc}(\mathbf{r}, \mathbf{s}, t = \tau_0), \qquad (33)$$

where $\tau_0 = (|\mathbf{x}-\mathbf{r}| + |\mathbf{x}-\mathbf{s}|)/c_0$. Setting $h = 0$ in this equation yields the 2-D version of equation (29). The migration formula for a 2-D fixed-source experiment (shot gather) can also be derived from equation (32) by computing the change of variables with $s = m - h$ fixed and $r = m + h$ varying over the surface line.

EXAMPLES

Next consider one analytical example and several numerical examples of migration by an inverse generalized Radon transform. The analytical example helps to clarify the notion of an approximate inversion that images discontinuities. The numerical examples are designed to show the resolution that can be obtained from different seismic experiments. Examples of generalized Radon transform migration of field data (offset vertical seismic profiles) can be found in Dupal and Miller (1985) and Miller and Dupal (1986).

Step-function increase in scattering potential

The analytical example consists of a zero-offset experiment on the surface of a half-space that has a step-function increase in the scattering potential. Consider the velocity function defined by the relation

$$c^{-2}(z) = 1 + \Theta(z - z_0),$$

where $\Theta(z)$ is the Heaviside step function and $z = z_0$ is the depth of the reflector. Taking $c_0^{-2} = 1$ gives the scattering potential

$$f(z) = \Theta(z - z_0).$$

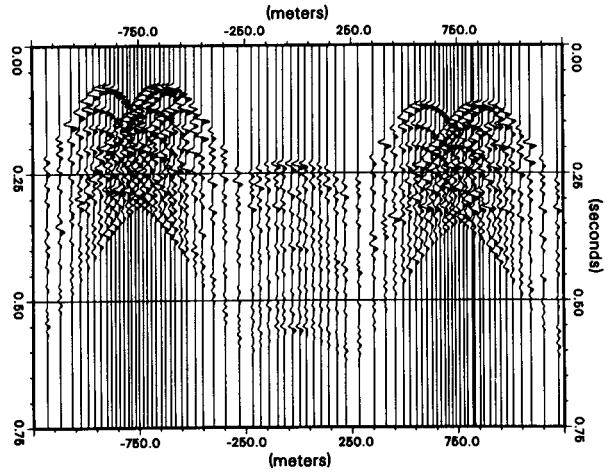

FIG. 11. Synthetic data from a zero-offset experiment with transceivers at the receiver locations in Figure 9. Traces are displayed in a coordinate system wrapped around the receiver set and centered on the source in Figure 9. The left borehole traces are positioned from −1250 to −250 m (1000 to 0 m actual depth), the surface traces from −250 to 250 m, and the right borehole traces are from 250 to 1250 m (0 to 1000 m actual depth). Every second trace is displayed. The scattering medium and the source wavelet were identical to those of Figure 9.

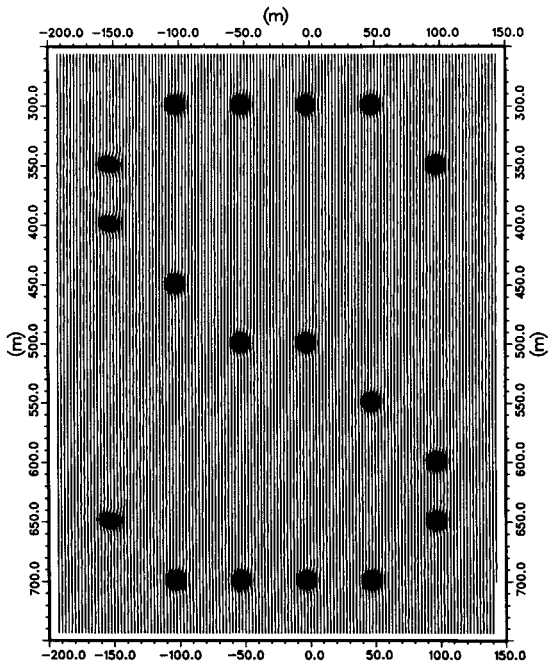

FIG. 12. Reconstruction from the data of Figure 11 using the inverse acoustic generalized Radon transform.

The scattered data within the Born approximation are easily computed from integrals of f over hemispheres. It follows from equation (14) that

$$u_{sc}(t) = -\frac{\partial^2}{\partial t^2}\,\Theta\hat{}(t),$$

where

$$\Theta\hat{}(t) = \frac{1}{2}\int_{I_t} d^2\mathbf{x}\,(2\pi t)^{-2}\Theta(\mathbf{x}_3 - z_0) = \frac{1}{32\pi^2}\int_{A_t} d^2\boldsymbol{\xi}.$$

Here, I_t is the spherical shell of radius $t/2$,

$$A_t = \{\boldsymbol{\xi}: |\boldsymbol{\xi}| = 1 \quad \text{and} \quad \xi_3 \geq 2z_0/t\}$$

is the region on the unit sphere similar to the intersection of I_t with the half-space $\{\mathbf{x}: x_3 \geq z_0\}$ (see Figure 8). Clearly $\Theta\hat{} = 0$ when $t < 2z_0$. Otherwise,

$$\Theta\hat{}(t) = \frac{1}{32\pi^2}\int_0^{\cos^{-1}(2z_0/t)} d\alpha\; 2\pi \sin\alpha = \frac{1}{16\pi}(1 - 2z_0/t).$$

Thus,

$$u_{sc}(t) = -\frac{1}{16\pi}\frac{\partial^2}{\partial t^2}\left[(1 - 2z_0/t)\Theta(t - 2z_0)\right]$$

$$= -\frac{1}{16\pi}\left[\frac{1}{2z_0}\,\delta(t - 2z_0) - \frac{4z_0\,\Theta(t - 2z_0)}{t^3}\right]. \tag{34}$$

Because of the symmetry in this example, it is easy to work directly with equation (27). However, an additional factor of 2 must be inserted in this equation since the integration over ξ will be taken only over a hemisphere. This still gives full

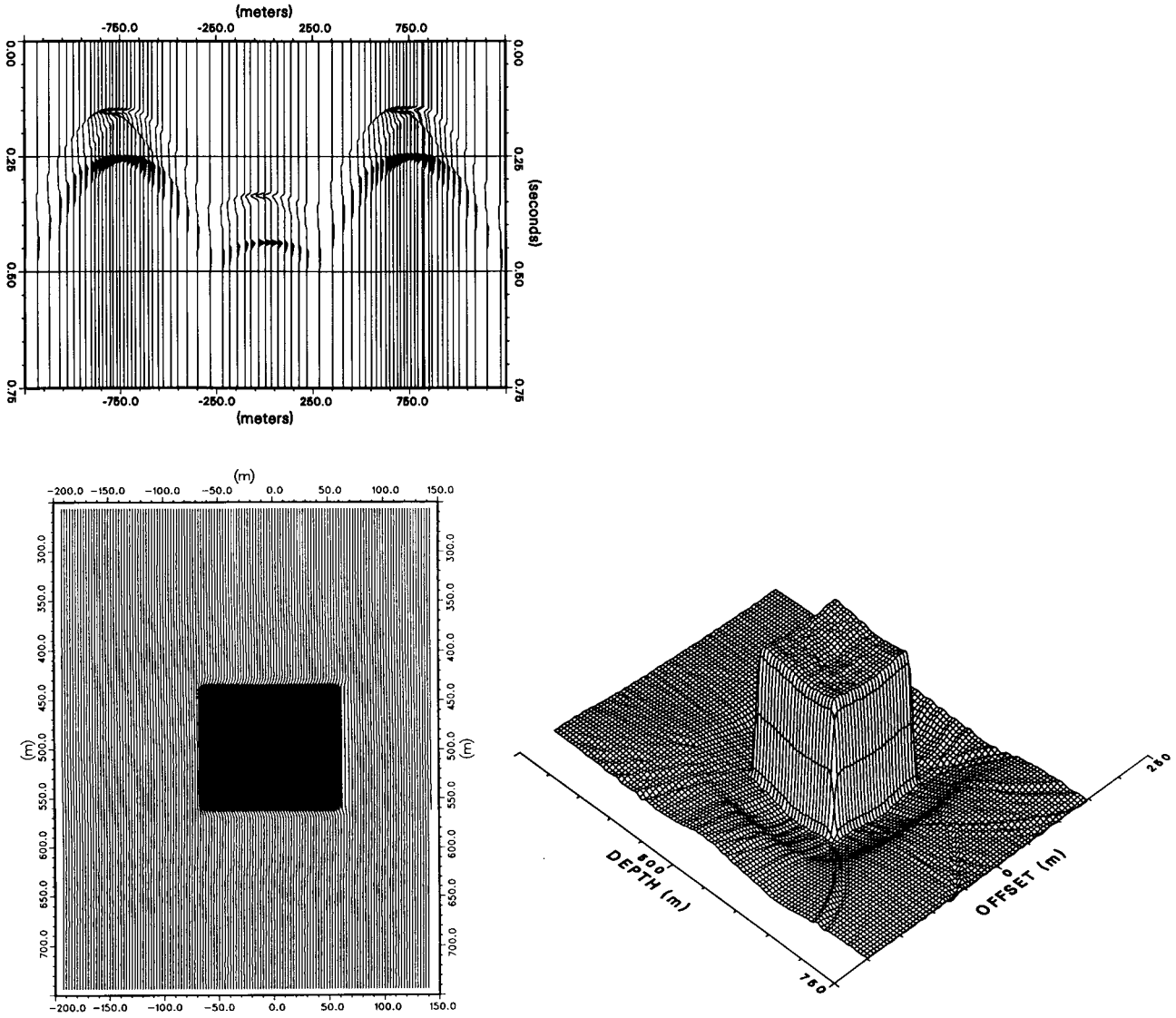

FIG. 13. (a) Synthetic zero-offset data for a homogeneous block occupying the object area of Figure 9. Data were computed with equation (12a) by representing the block as a fine grid of point objects. The display geometry is the same as in Figure 11. (b) Reconstructed block: (left) wiggle plot; (right) perspective view.

coverage of tangent planes passing through an image point; integration over the full sphere implies double coverage of the tangent planes. The amplitude factor is $(4\pi r)^{-2}$, and the obliquity factor is unity. Thus

$$\langle f(z)\rangle = \frac{2}{\pi^2}\int d^2\xi(16\pi r^2)u_{sc}(t=2r)$$
$$= -\frac{2}{\pi}\int_0^{2\pi} d\phi \int_0^{\pi/2} d\theta \sin\theta\, r^2$$
$$\times\left[\frac{1}{2z_0}\delta(2r-2z_0) - \frac{z_0\Theta(2r-2z_0)}{2r^3}\right].$$

The change of variables $\cos\theta = z/r$ yields

$$\langle f(z)\rangle = \frac{z_0}{z}\Theta(z-z_0). \tag{35}$$

The location and size of the discontinuity are recovered exactly, but the value for f itself decays by the smooth function z_0/z away from the interface. A similar result would be obtained if a more accurate expression for the data were substituted into the inversion formula (this example was suggested to us at the 1985 International Meeting of the SEG by Richard Day who performed a similar calculation using the data given by geometrical optics). Since inverse scattering is linear in the Born approximation, the result is easily extended to an arbitrary number of interfaces. For example, in the case of two interfaces, by setting the scattering potential to be

$$f(z) = \Theta(z-z_0) - \Theta(z-z_0-a),$$

where a is the thickness of the layer, within the Born approximation

$$\langle f(z)\rangle = \frac{z_0}{z}\Theta(z-z_0) - \frac{z_0+a}{z}\Theta(z-z_0-a).$$

The discontinuities are again recovered exactly. Moreover, for fixed z, the value of the reconstruction has the correct limiting value as the layer thickness approaches zero. If exact data are used in the multilayer case, the locations of deeper interfaces may not be positioned correctly, since they will "migrate" with the background velocity c_0. This is a well-known defect of linearized inversion.

Synthetic examples: Surface and borehole data

Figures 9 through 16 show four synthetic examples of the acoustic GRT migration algorithm specialized to a 2-D geometry. In performing the first three synthetic experiments, we used equation (12a) to generate the data and equation (27a) to perform the reconstructions. These examples were performed with a homogeneous background velocity. The source wavelet was a four-point Blackman-Harris window (Harris, 1978, p. 65), which resembles a band-limited delta function.

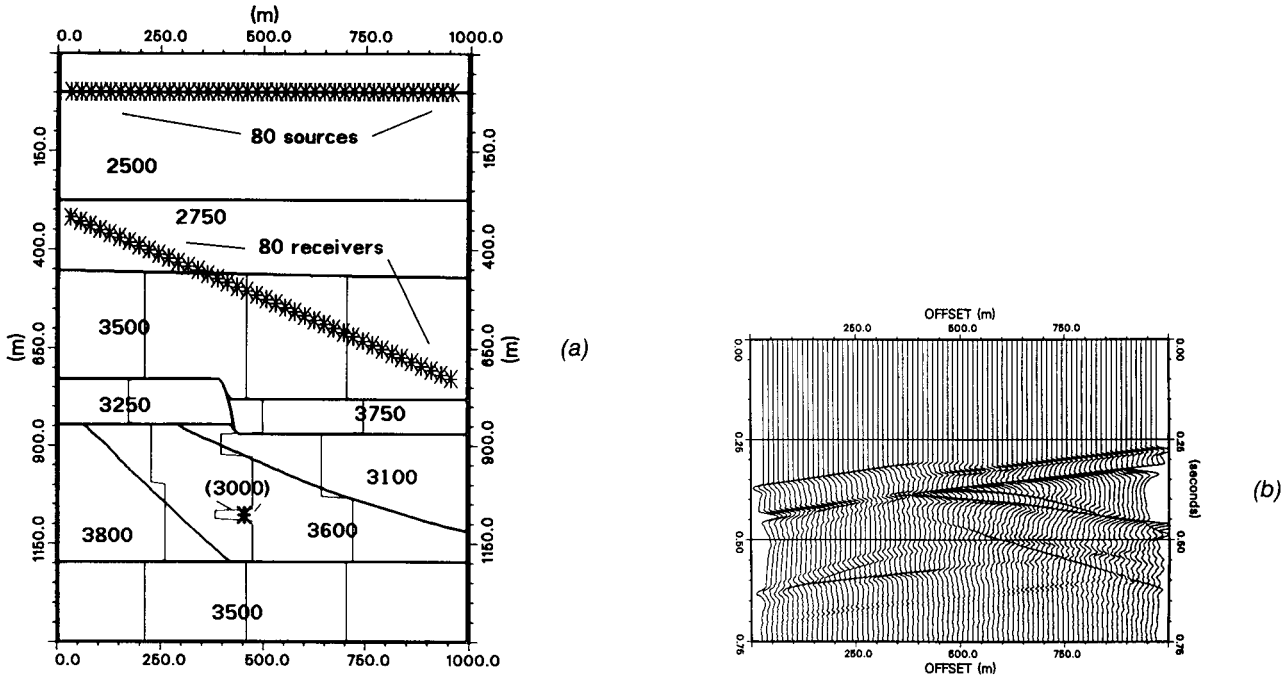

FIG. 14. Synthetic deviated-well VSP experiment. (a) The acoustic model consisted of a family of faulted and dipping layers with a point anomaly at $(x, z) = (454, 1076)$ m. Three vertical traces graph the scattering potential relative to a background model, consisting of the flat cross-section of the true model at the borehole (2500 m/s above $z = 275$ m, 2750 m/s between 275 and 460 m, 3500 m/s below 460 m). (b) The scattered data, consisting of time traces for 80 source-receiver pairs. Each trace is the difference between a total-field trace and a background-field trace computed by a pair of finite-difference simulations for the corresponding source point.

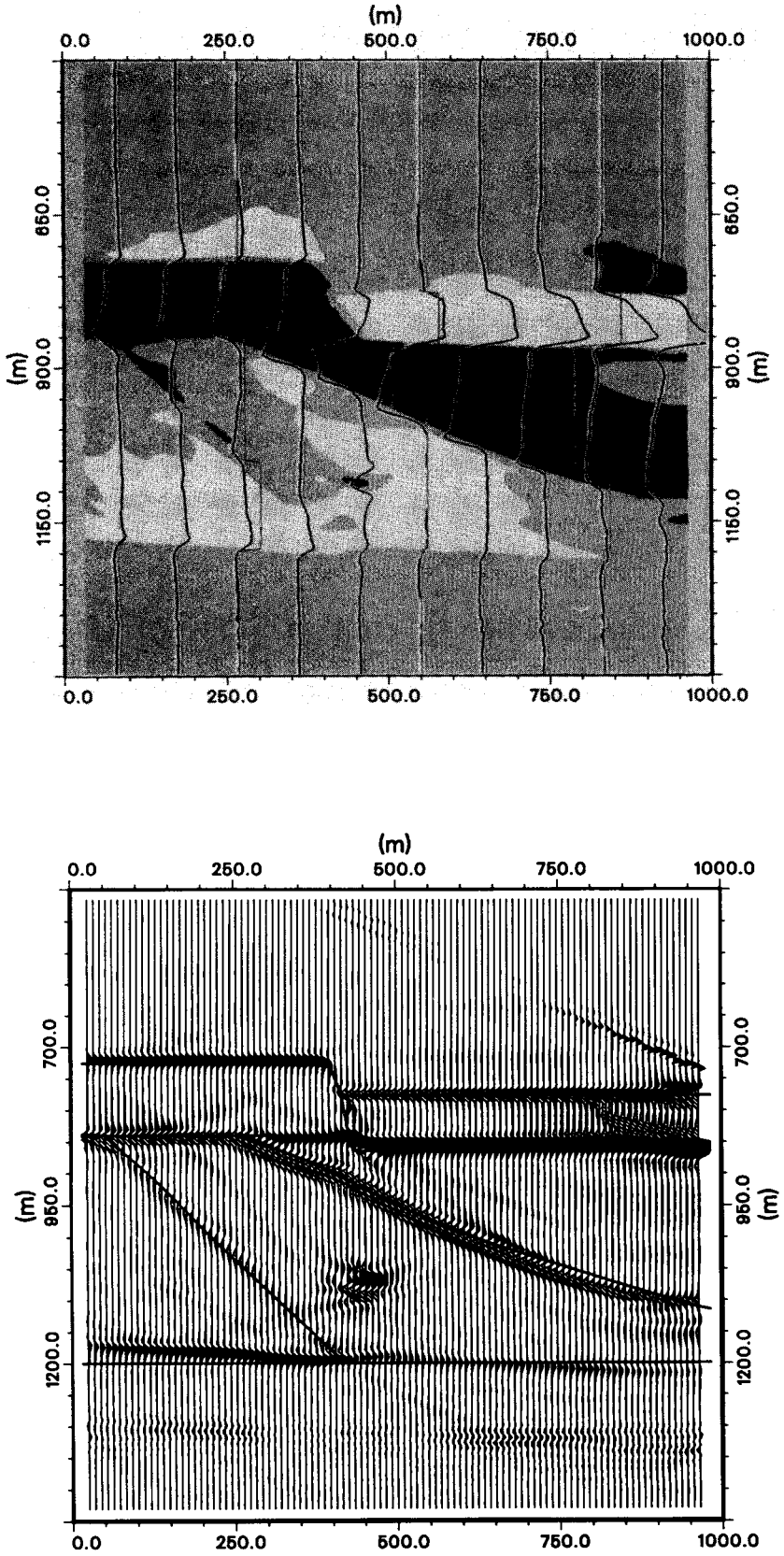

FIG. 15. Reconstruction from the synthetic DVSP experiment. (a) Ten wiggle plots showing profiles of the reconstructed scattering potential are superimposed on a gray-level display of the same image. Vertical profiles of the true scattering potential are shown at $x = 260$, 600, and 840 m. (b) Wiggle display of the vertical derivative of the previous image. Layer boundaries from the true model are superimposed.

The first example consists of data for a single-source, multiple-receiver experiment with the source and receivers arranged as in Figure 1. The scattering object consisted of a family of point scatterers, which were separated by roughly one wavelength at the central frequency of the source and distributed to form the letter "S." Figure 10 shows the synthetic data after application of the Hilbert transform. The reconstructed images in Figure 10 illustrate the resolution obtained from different subsets of the data.

The second and third examples involve data from zero-offset experiments in which transceivers are placed at the receiver locations of Figure 1. The scattering objects were the same family of point objects and a homogeneous block. Figures 11 and 13a show the synthetic data, while Figures 12 and 13b show the corresponding reconstructions.

The final example is a bit closer to real life. The geometry of the experiment has been described as a "vertical raypath deviated-well VSP" (DVSP for short). In this type of survey, the receiver moves up a deviated borehole, while the source moves along the surface directly above the receiver; that is, for $\mathbf{r} = (r_1, r_2, r_3)$, $\mathbf{s} = (r_1, r_2, 0)$. This type of experimental geometry is easily handled by a direct application of the basic inversion algorithm. We know of no other wave-equation method that can treat this geometry.

The model is shown in Figure 14a. It consists of faulted and dipping layers, plus a point anomaly at the position $(x, z) = (454, 1076)$ m. The background model was layered, with the velocities along the well extended laterally; the velocity at the deepest part of the well was extended downward. By running a 2-D acoustic finite-difference program 160 times, synthetic scattered data were obtained for 80 source-receiver pairs. The source wavelet was a Blackman-Harris window with a duration of 21.3 ms (which contains frequencies ranging from 0 to about 50 Hz).

Figure 15a shows the reconstructed image using a direct implementation of equation (27a). To simplify computation, straight raypaths were used to compute all geometric factors (including $d\xi$), and slowness in the layered background was integrated along straight rays to compute traveltimes. Figure 15b shows the vertical derivative of the image in Figure 15a, superimposed on the model. A similar result could be obtained by differentiating the data before inversion.

Note that all boundaries are recovered with the correct polarity. The shallow faulted layers are located very accurately. It is particularly interesting to note the accurate reconstruction of amplitudes in and around the wedge-shaped region between 150 and 500 m offset, just below the faulted layers (850 to 950 m). The reconstructed shapes of the dipping layers and the deepest flat layer show some distortion due to the breakdown of the Born approximation. The loss in amplitude at the bottom of the leftmost dipping layer results from a lack of illumination. The loss of amplitude on the deepest flat layer as it intersects the dipping boundary is physically correct and is due to the change in velocity contrast at that point.

CONCLUSIONS

We have described an integral-transform approach to seismic imaging that formalizes the classical diffraction stack. The basis of this approach is that acoustic scattering transforms the scattering potential into the data as integrals over isochron surfaces; in turn, integrating the data over dual surfaces recovers an image of the scattering potential. Since the experimental geometry and the velocity model enter only in deter-

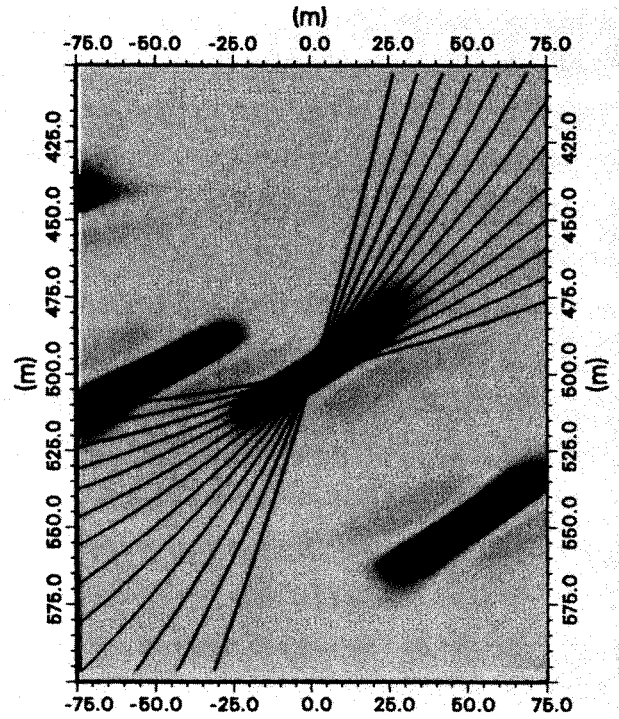

FIG. 16. Typical point from Figure 10c (left well only) together with the family of isochron surfaces corresponding to data points on the associated reflection-time surface. Every fifth isochron is plotted.

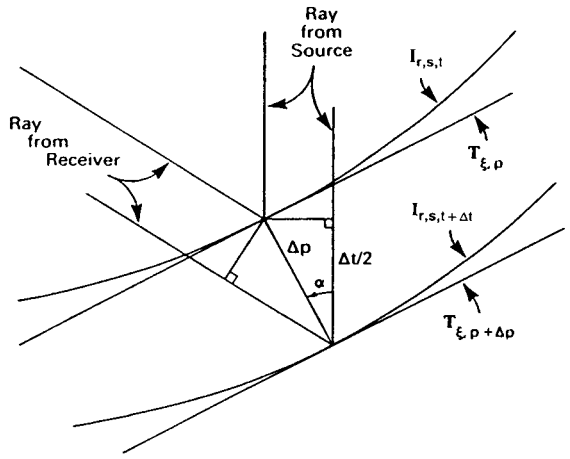

FIG. 17. Geometry that translates the time variable t into distance p normal to an isochron surface. Parallel isochron surfaces satisfy the relation

$$\cos \alpha = \frac{c_0(\mathbf{x}_0)\Delta t}{2\Delta p}.$$

To simplify the figure, we have set $c_0(\mathbf{x}_0) = 1$.

mining the shapes and locations of the surfaces, the method is easily adapted to general source-receiver geometries and velocity models. Moreover, the dependence of spatial resolution on the geometry of the experiment, the reconstruction algorithm, and the assumptions about the medium is explicit in this method. It is thus possible to analyze the differences in performing just surface experiments, just borehole experiments, or both. It is also possible to describe an ideal experiment for a given configuration.

Analysis of the spatial resolution of seismic experiments and migration (or inversion) algorithms was treated in detail in Beylkin et al. (1985) (this paper also shows that the integral-transform approach can be modified to resemble a full wavefield extrapolation approach).

We conclude by pointing out the main geometric issues affecting the spatial resolution of the images obtained by the inverse acoustic generalized Radon transform. For example, the difference between Figure 10a and Figure 12 raises questions regarding the angular resolution of a band-limited variable-offset experiment. These issues involve both the experimental geometry and the finite bandwidth of the source wavelet.

The first issue is the relation between the available source-receiver pairs and the spatial dip spectrum of the reconstructed object. Locally, a restriction on the number of source points or receiver points restricts the set of available isochron surfaces in the generalized Radon transform, and hence, the set of tangent planes (parameterized by ξ) available at each image point. Recall from the discussion of the classical Radon transform that integrals over planes in all directions are needed for a perfect reconstruction. Figure 15 shows a typical point from the image in Figure 10d, together with the set of isochron surfaces passing through that point. Roughly, the image spreads along the isochron surfaces. Comparison of the images in Figure 10 shows the effect of restricting the receiver set, and thus the dip spectrum at image points, while keeping other factors constant.

The difference between the two full-aperture images, Figures 10a and 12, is due to a more subtle effect. The correspondence that relates the time variable t at a typical data point $(\mathbf{r}, \mathbf{s}, t)$ to

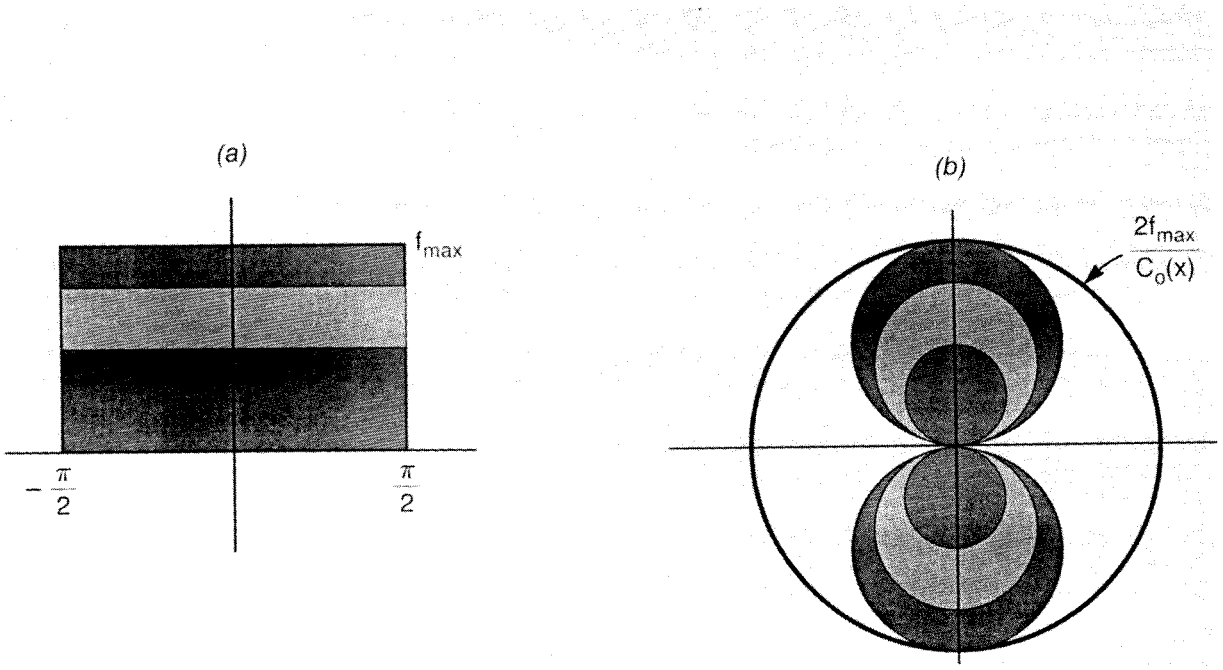

FIG. 18. Spatial Fourier-domain coverage for a 2-D band-limited experiment. (a) Data from a finite-bandwidth, full-aperture experiment cover the angular aperture $-\pi/2 \le \theta \le \pi/2$ at an image point, where θ is the angle that parameterizes ξ, the unit vector normal to tangent planes (lines) through the image point. This range of θ gives single coverage of all tangent planes. Frequencies vary from zero to the maximum frequency in the source wavelet. (b) The region of coverage in (a) when mapped into the domain of (local) spatial frequencies $\mathbf{k} = (k_x, k_z)$ near an image point. In a zero-offset experiment, the coverage of spatial frequencies is the region enclosed by the outer circle, which is defined by the polar equation

$$r = |\mathbf{k}| = \frac{2f_{max}}{c_0(\mathbf{x}_0)}.$$

In a fixed-source experiment, the coverage is the region enclosed by the figure eight (shaded dark and light). In this case, taking $\theta = 0$ for the zero-offset receiver makes $\theta = \alpha$, half the angle between the incident and scattered rays at an image point [see Figure 15 and equation (36)]. The limit of coverage is defined by the polar equation

$$r = |\mathbf{k}| = \frac{2f_{max}}{c_0(\mathbf{x}_0)} \cos\theta,$$

where the top and bottom portions of the figure eight come from positive and negative temporal frequencies $\pm f_{max}$. The shading in (a) and (b) illustrates the distortion of different frequency bands under the mapping.

the local spatial variable p normal to the corresponding isochron surface is [see Figure 17 and equation (23)]

$$\Delta p = \frac{c_0(\mathbf{x}_0)}{2\cos\alpha}\,\Delta t. \tag{36}$$

A minimal time step in the data, corresponding to the highest available temporal frequency, translates to a minimal spatial step that varies as 1/cos of the scattering angle and, hence, to a highest spatial frequency that varies as the cosine of the scattering angle. In a zero-offset experiment (as in Figure 12), this obliquity factor is constant, and the point spreads are symmetric. In a fixed-source experiment (as in Figure 10), the obliquity factor varies with scattering angle and the point spreads are ovals, with their minor axes aligned toward the source.

Figure 18 shows the predicted areas of coverage in the Fourier domain for the two cases, while Figure 19 shows Fourier transforms of actual reconstructions from single-point synthetic experiments similar to the ones that produced Figures 10a and 12. Figure 20 shows a typical point from Figure 10a, together with the family of isochrons corresponding to data points one-half wavelength from the associated reflection-time surface. This last figure illustrates the obliquity effect directly in the image domain.

The mapping of the data into the spatial Fourier spectrum of the object, shown in Figures 18 and 19, is a local version of a relationship first pointed out by Wolf (1969) in the context of holographic imaging. With a harmonic plane-wave source, the spatial Fourier transform of the scattered field recorded along a line can be related to the Fourier transform of the object along a circular trajectory in the Fourier domain. This relationship forms the basis of diffraction tomography (Devaney, 1982) and is implicit in migration by Fourier transform (Stolt, 1978). The integral transform approach in the acoustic generalized Radon transform, and the theory of Fourier integral operators which underlies it, simply provide a convenient formalism for localizing the relationship around image points and for analyzing the errors caused by the localization.

Finally, the interpretation of acoustic scattering at high frequencies as a generalized Radon transform does not require use of the linearized (Born) scattering approximation. If

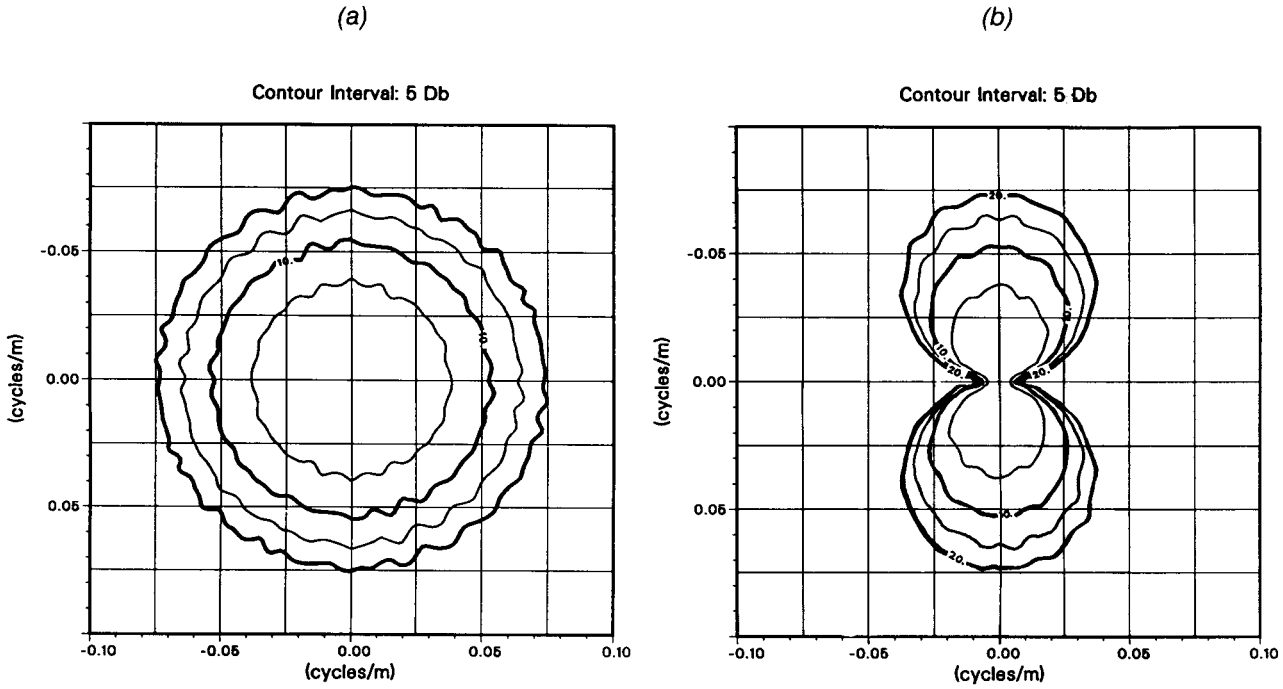

FIG. 19. (a) Fourier transform of the image obtained from a one-point, zero-offset experiment similar to the experiment that produced Figure 12. (b) Fourier transform of the image obtained from a one-point, fixed-source experiment similar to the experiment that produced Figure 10a. The wavelet was identical to the one used in Figures 9, 11, and 13. Sample waveforms (after Hilbert transform) are shown in Figure 20. The plots show amplitude contours at levels -5, -10, -15, -20 dB with respect to the peak amplitude in the file. The Fourier coverage obtained in these numerical experiments should be compared with the theoretical coverage shown in Figure 18. The peak spatial frequency of .075 cycles/m for the -20 dB contours corresponds to a cutoff temporal frequency of 94 cycles/s.

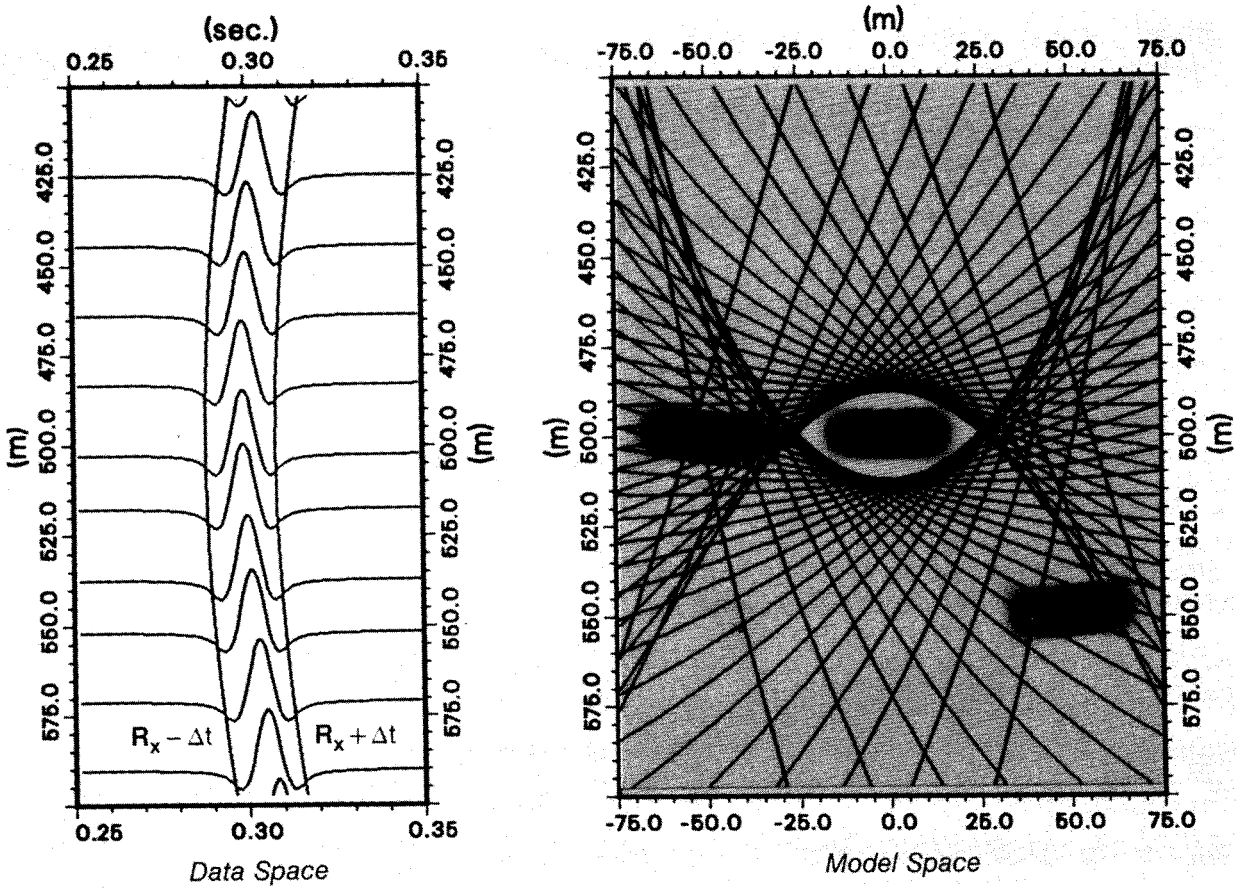

FIG. 20. A typical point from Figure 10a together with the family of isochron surfaces corresponding to data points 1 ms from the associated reflection-time surface R_x. The isochron surfaces corresponding to $R_x - \Delta t$ form the family above the image point, while the isochron surfaces corresponding to $R_x + \Delta t$ form the family below the image point. Every fifth isochron surface is shown. $\Delta t = .01$ s is one half-wavelength for a signal at 50 Hz (which is roughly the dominant frequency in the Hilbert-transformed and differentiated wavelet). It corresponds to a peak spatial frequency of .04 cycles/m in Figure 19b.

geometrical-optics approximations are used for G_0 and u in the exact equation (7), one obtains an acoustic generalized Radon transform similar to equation (12). However, the traveltime and amplitude terms along the incident raypath are then governed by the true velocity $c(\mathbf{x})$. These terms are, of course, unknown, which is just another illustration of the nonlinearity of the inverse problem.

ACKNOWLEDGMENTS

F. Mons and K. Babour (Études et Productions Schlumberger, France) suggested the problem of doing wave-equation migration with VSP data. Discussions with them helped greatly to clarify the ideas presented here. A. Devaney (Schlumberger-Doll Research) and R. Clayton (California Institute of Technology) provided valuable insights into Born inversion and Kirchhoff migration. R. Wiggins (Schlumberger-Doll Research) supported the work from beginning to end.

REFERENCES

Berkhout, A. J., 1984, Multidimensional linearized inversion and seismic migration: Geophysics, **49**, 1881–1895.

Beylkin, G., 1982, Generalized Radon transform and its applications: Ph.D. Thesis, New York Univ.

——— 1984, The inversion problem and applications of the generalized Radon transform: Comm. Pure Appl. Math., **37**, 579–599.

——— 1985, Imaging of discontinuities in the inverse scattering problem by inversion of a causal generalized Radon transform: J. Math. Phys., **26**, 99–108.

Beylkin, G., and Oristaglio, M., 1985, Distorted-wave Born and distorted-wave Rytov approximations: Optics Comm., **53**, 213–215.

Beylkin, G., Oristaglio, M., and Miller, D., 1985, Spatial resolution of migration algorithms, *in* Berkhout, A. J., Ridder, J., and van der Waal, L. F., Eds., Acoustical Imaging, **14**, Plenum Pub. Co., 155–167.

Bleistein, N., and Gray, S. H., 1985, An extension of the Born inversion method to a depth dependent reference profile: Geophys. Prosp., **33**, 999–1022.

Claerbout, J. F., 1971, Toward a unified theory of reflector mapping: Geophysics, **36**, 467–481.

Claerbout, J. F., and Doherty, S. M., 1972, Downward continuation of moveout corrected seismograms: Geophysics, **37**, 741–768.

Clayton, R. W., and Stolt, R. H., 1981, A Born-WKBJ inversion method for acoustic reflection data: Geophysics, **46**, 1559–1567.

Deans, S. R., 1983, The Radon transform and some of its applications: J. Wiley & Sons, Inc.

Devaney, A. J., 1982, A filtered-backpropagation algorithm for diffraction tomography: Ultrasonic Imaging, **4**, 336–350.

Devaney, A. J., and Oristaglio, M., 1984, Inversion procedure for inverse scattering within the distorted-wave Born approximation: Phys. Rev. Lett., **51**, 237–240.

Dupal, L., and Miller, D. E., 1985, Reef delineation by multiple offset

borehole seismic profiles: A case study: Presented at the 55th Ann. Internat. Mtg., Soc. Explor. Geophys., Washington, D. C.,; abstracts and biographies 105–107.
Fawcett, J. A., 1985, Inversion of n-dimensional spherical averages: Soc. Ind. Appl. Math., **45**, 336–341.
French, W. S., 1974, Two-dimensional and three-dimensional migration of model-experiment reflection profiles: Geophysics, **39**, 265–277.
——— 1975, Computer migration of oblique seismic reflection profiles: Geophysics, **40**, 961–980.
Gardner, G. H. F., Ed., 1985, Migration of seismic data: Geophysics reprints series, no. **4**, Soc. Explor. Geophys.
Gardner, G. H. F., French, W. S., and Matzuk, T., 1974, Elements of migration and velocity analysis: Geophysics, **39**, 811–825.
Gazdag, J., and Sguazzero, P., 1984, Migration of seismic data: Proc. Inst. Electr. Electron. Eng., **72**, 1302–1315.
Gel'fand, I. M., and Shilov, G. E., 1966, Generalized functions: **1**, Properties and operations: Academic Press, Inc.
Gel'fand, I. M., Graev, M. I., and Vilenkin, N. Ya., 1966, Generalized functions: **5**, Integral geometry and representation theory: Academic Press, Inc.
Gel'fand, I. M., Graev, M. I., and Shapiro, Z. Ya, 1969, Differential forms and integral geometry: Functional Anal. Appl., **3**, 24–40.
Hagedoorn, J. G., 1954, A process of seismic reflection interpretation: Geophys. Prosp., **2**, 85–127.
Harris, F. J., 1978, On the use of windows for harmonic analysis with the discrete Fourier transform: Proc., Inst. Electr. Electron. Eng., **66**, 51–83.
Helgason, S., 1984, Groups and geometric analysis: Integral geometry, invariant differential operators, and spherical functions: Academic Press, Inc.
Herman, G. T., 1980, Image reconstruction from projections: Academic Press, Inc.
Johnson, J. D., and French, W. S., 1982, Migration—The inverse method, *in* Jain, K. C., and deFigueiredo, R. J. P., Eds., Concepts and techniques in oil and gas exploration: Soc. Explor. Geophys.
Lindsey, J. P., and Hermann, A., 1970, Digital migration: Oil and Gas J., **38**, 112–115.
Miller, D. E., 1983, Integral transforms and the migration of multiple-offset borehole seismic profiles: Research Note, Schlumberger-Doll Research.
Miller, D. E., and Dupal, L., 1986, Reef delineation by multiple offset borehole seismic profiles: A case study: Geophysics, submitted.
Miller, D., Oristaglio, M., and Beylkin, G., 1984, A new formalism and old heuristic for seismic migration: Presented at the 54th Ann. Int. Mtg., Soc. Explor. Geophys., Atlanta; abstracts and biographies, 704–707.
Norton, S. G., and Linzer, M., 1981, Ultrasonic scattering potential imaging in three dimensions: Exact inverse scattering solutions for plane, cylindrical, and spherical apertures: Inst. Electr. Electron. Eng. Trans. on Biomedical Engineering, **BME-28**, 202–220.
Quinto, E., 1980, The dependence of the generalized Radon transform on defining measures: Trans., Am. Math. Soc., **257**, 331–346.
Radon, J., 1917, Über die Besttimmung von Funktionen durch ihre Integralwerte längs gesisser Mannigfaltigkeiten: Ber. Verh. Sächs. Akad., **69**, 262–277.
Robinson, E. A., 1983, Migration of geophysical data: Internat. Human Res. Dev. Corp.
Rockwell, D. W., 1971, Migration stack aids interpretation: Oil and Gas J., **69**, 202–218.
Schneider, W. A., 1971, Developments in seismic data processing and analysis (1968–1970): Geophysics, **36**, 1043–1073.
——— 1978, Integral formulation for migration in two and three dimensions: Geophysics, **43**, 49–76.
Schultz, P. S., 1976, Velocity estimation by wavefront synthesis: Ph.D. thesis, Stanford Univ.
Stolt, R. H., 1978, Migration by Fourier transform: Geophysics, **43**, 23–48.
Stolt, R. H., and Weglein, A. B., 1985, Migration and inversion of seismic data: Geophysics, **50**, 2458–2472.
Tarantola, A., 1984, Inversion of seismic reflection data in the acoustic approximation: Geophysics, **49**, 1259–1267.
Taylor, J. R., 1972, Scattering theory: John Wiley and Sons, Inc.
Wolf, E., 1969, Three-dimensional structure determination of semi-transparent objects from holographic data: Optics Comm., **1**, 153–156.

APPENDIX

Formula (27) was derived within the linearized inverse problem under the following additional assumptions:

(1) the function $f(\mathbf{x})$ is localized around the point $\mathbf{x}_0$;
(2) isochron surfaces can be approximated by tangent planes in the neighborhood of the point $\mathbf{x}_0$; and
(3) the change of variables which results in the construction of the weight function [equation (26)] exists.

Analysis of these assumptions is helpful in explaining the meaning of reconstructions via formula (27). For a more detailed discussion of these questions, see Beylkin (1985).

Start with assumption (3). The construction of the weight function is essentially a change of variables. This means that to be valid, the corresponding Jacobian has to be nonzero. This condition has a clear geometrical and physical interpretation. When isochron surfaces are replaced by tangent planes, we assume that these tangent planes are different for different isochron surfaces. Also, for technical purposes, we assume that from one isochron surface to another the change in the directions of the normals to their tangent planes is continuous. This condition is always satisfied for a constant reference velocity and boundaries which are "star shaped" with respect to the point of reconstruction. For variable reference velocities, this condition might not be satisfied; it thus becomes one of our assumptions.

Now turn to assumptions (1) and (2). If the function $f(\mathbf{x})$ is not localized around the point $\mathbf{x}_0$, the difference between the reconstructed function and the original one is infinitely smooth; i.e., the discrepancy has an infinite number of derivatives. This discrepancy does not have to be small, in general, but when the curvatures of isochron surfaces are small, this discrepancy is also small. The replacement of isochron surfaces by planes in the neighborhood of the point of reconstruction causes an error that has at least one derivative more than the function that is being reconstructed. Also, when curvatures are small, this error is also small.

Accurate proof of these statements requires analysis of a Fourier integral operator, which appears when one substitutes expression (12) for the scattered field into equation (27),

$$\langle f(\mathbf{x}_0)\rangle = -\frac{1}{\pi^2}\int d^3\mathbf{x}\int d^2\xi\,\frac{|\cos^3\alpha|\,A(\mathbf{r},\mathbf{x},\mathbf{s})}{c_0^3(\mathbf{x}_0)A(\mathbf{r},\mathbf{x}_0,\mathbf{s})} \times \delta''\Big[\tau(\mathbf{r},\mathbf{x}_0,\mathbf{s})-\tau(\mathbf{r},\mathbf{x},\mathbf{s})\Big]f(\mathbf{x}),$$

and then replaces the second derivative of the delta function

by its Fourier integral, yielding

$$\langle f(\mathbf{x}_0)\rangle = \frac{1}{2\pi^3}\int d^3\mathbf{x}\int d^2\xi\int d\omega\,\omega^2\,\frac{|\cos^3\alpha|\,A(\mathbf{r},\mathbf{x},\mathbf{s})}{c_0^3(\mathbf{x}_0)A(\mathbf{r},\mathbf{x}_0,\mathbf{s})} \times \exp\left\{i\omega\left[\tau(\mathbf{r},\mathbf{x}_0,\mathbf{s})-\tau(\mathbf{r},\mathbf{x},\mathbf{s})\right]\right\}f(\mathbf{x}), \quad \text{(A-1)}$$

where $d^2\xi = d^2\xi(\mathbf{r},\mathbf{x}_0,\mathbf{s})$ and $\alpha = \alpha(\mathbf{r},\mathbf{x}_0,\mathbf{s})$. The inner integrals in equation (A-1) can be interpreted as an approximate construction of the 3-D delta function by integration over 3-D Fourier space in spherical coordinates (ξ, ω) with measure $d^2\xi d\omega\,\omega^2$. If the integrals in (A-1) are taken over an arbitrary bounded (compact) region in Fourier space instead of over the whole space, then the resulting function will have derivatives of all orders. This essentially follows from the fact that the integrals which express these derivatives exist. For large ω, one can thus apply stationary-phase arguments to the expression inside the integrals. A (first-order) stationary-phase analysis will account for contributions from the point $\mathbf{x}_0$, giving $f(\mathbf{x}_0)$. It can be shown, moreover, that the second-order and higher-order terms in the Taylor expansion of the phase function, together with the first-order and higher-order terms in the Taylor expansion of the amplitude, give a total error that has at least one derivative more than the function to be reconstructed.

Since the error is smooth, it follows that the discontinuities (surfaces of discontinuity) of the scattering potential $f(\mathbf{x})$ are reconstructed reliably. In other words, the positions of these discontinuities and also the jumps at these discontinuities are recovered, within the limits of the linearized approximation to inverse scattering.